Bioactive Materials 43 (2025) 376–391

Contents lists available at ScienceDirect

Bioactive Materials

journal homepage: www.keaipublishing.com/en/journals/bioactive-materials

Tailored polysaccharide entrapping metal-organic framework for RNAi therapeutics and diagnostics in atherosclerosis

Sen Li [a,1], Han Gao [b,c,1,**], Haoji Wang [d,e], Xiaolin Zhao [d], Da Pan [f], Idaira Pacheco-Fernández [b], Ming Ma [d,e], Jianjun Liu [d], Jouni Hirvonen [c], Zehua Liu [b,c,***], Hélder A. Santos [b,c,*]

[a] Department of Vascular Surgery, The Second Affiliated Hospital, Zhejiang University School of Medicine, Hangzhou 310009, China
[b] Department of Biomaterials and Biomedical Technology, The Personalized Medicine Research Institute (PRECISION), University Medical Center Groningen (UMCG), University of Groningen, Ant. Deusinglaan 1, 9713 AV, Groningen, the Netherlands
[c] Drug Research Program, Division of Pharmaceutical Chemistry and Technology, Faculty of Pharmacy, University of Helsinki, Helsinki, FI-00014, Finland
[d] State Key Laboratory of High Performance Ceramics and Superfine Microstructures, Shanghai Institute of Ceramics, Chinese Academy of Sciences, Shanghai, 200050, PR China
[e] School of Chemistry and Materials Science, Hangzhou Institute for Advanced Study, University of Chinese Academy of Sciences, Hangzhou, 310024, PR China
[f] Key Laboratory of Environmental Medicine and Engineering of Ministry of Education, and Department of Nutrition and Food Hygiene, School of Public Health, Southeast University, Nanjing, 210009, PR China

ARTICLE INFO

Keywords:
Polysaccharide
Gene therapy
RNAi therapeutics
Atherosclerosis
Metal-organic framework

ABSTRACT

Metal-organic frameworks (MOFs) hold promise as theranostic carriers for atherosclerosis. However, to further advance their therapeutic effects with higher complexity and functionality, integrating multiple components with complex synthesis procedures are usually involved. Here, we reported a facile and general strategy to prepare multifunctional anti-atherosclerosis theranostic platform in a single-step manner. A custom-designed multifunctional polymer, poly(butyl methacrylate-co-methacrylic acid) branched phosphorylated β-glucan (PBMMA-PG), can effectively entrap different MOFs via coordination, simultaneously endow the MOF with enhanced stability, lesional macrophages selectivity and enhanced endosome escape. Sequential ex situ characterization and computational studies elaborated the potential mechanism. This facile post-synthetic modification granted the administered nanoparticles atherosclerotic tropism by targeting Dectin-1^{+} macrophages, enhancing in situ MR signal intensity by 72 %. Delivery of siNLRP3 effectively mitigated NLRP3 inflammasomes activation, resulting a 43 % reduction of plaque area. Overall, the current study highlights a simple and general approach for fabricating a MOF-based theranostic platform towards atherosclerosis conditioning, which may also expand to other indications targeting the lesional macrophages.

1. Introduction

Despite recent efforts on improving disease outcomes, atherosclerosis (AS) is still a major cause of morbidity and mortality worldwide [1]. Growing evidences demonstrated the perturbations of immune homeostasis instigates chronic inflammation and drives the formation of atherosclerotic plaques in the vessel wall [2]. Among which, macrophages are identified as key regulators of the immuno-pathological processes, with continuous novel anti-inflammatory therapies developed to further reduce the risk of cardiovascular incidences [3]. Nonetheless, these efforts are usually impeded by low bioavailability, limited target selectivity and substantial systematic toxicity associated with conventional anti-inflammatory medications [4–6]. Moreover, with the growing identification of new therapeutic targets lacking available drugs, gene therapy holds the theoretical potential as a robust approach to restore mutational genetic conditions [7]. Therefore, a versatile and effective strategy for precise genetic modulation of AS macrophages is in great demands [8].

Peer review under responsibility of KeAi Communications Co., Ltd.
* Corresponding author.
** Corresponding author.
*** Corresponding author.
E-mail addresses: h.gao@umcg.nl (H. Gao), zehua.liu@helsinki.fi (Z. Liu), h.a.santos@umcg.nl (H.A. Santos).
[1] These authors contributed equally.

https://doi.org/10.1016/j.bioactmat.2024.08.041
Received 30 May 2024; Received in revised form 26 August 2024; Accepted 29 August 2024

Nanotechnology offers unique advantages in tackling aforementioned challenges [9]. Yet, the effectiveness of such approaches necessitates a meticulous design and selection of nanomaterials with collaborative multifunctionalities, tailored to align with the pathological characteristics and treatment strategies of AS. Among many MOFs, iron (III) based MOFs (Fe MOFs) have garnered extensive attention in biomedical applications, which is attributed to the advantages of their relatively low toxicity and abundant availability in the earth [10–12]. Concurrently, owing to the inherent catalytic activity, Fe-based transition metals have been employed as artificial nanozymes, demonstrating capabilities such as peroxidase-like activity and biosensing [13]. In this perspective, Fe MOFs hold great potential as robust nanoplatforms for advancing gene delivery in AS.

However, unmodified MOFs have still major clinical translation hurdles, such as poor stability, potential toxicity, suboptimal endosome escape capability and lack of targeting selectivity [14–17]. Consequently, all these issues can lead to undesired off-targets effects and compromised MOF's efficiency in the intracellular delivery of genetic cargos. Different strategies and materials, including polymers [18–20], phospholipids [21,22], and biomacromolecules [23], have been successfully employed to modify the external surfaces of various MOFs, leading to the creation of nanohybrids to solve the aforementioned issues. Despite the progressive achievements, the attainment of higher complexity and enhanced functionality in MOFs typically demands the incorporation of multiple components and complex synthetic scheme [23,24]. Therefore, developing a strategy to simplify the creation of MOF-based nanosystems for AS genetic therapy holds great value.

Previous studies proposed a post-synthetic manner to modify the external surface of MOF via coordinative binding. For example, many hydroxy-rich biopolymers, such as cyclodextrin and alginate [25–27], have been reported to coordinate to the open metal centers in MOFs for improving the colloidal stability and cellular uptake. In addition, due to the strong binding affinity between metal ions and phosphate, previous studies reported the surface modification of MOF with

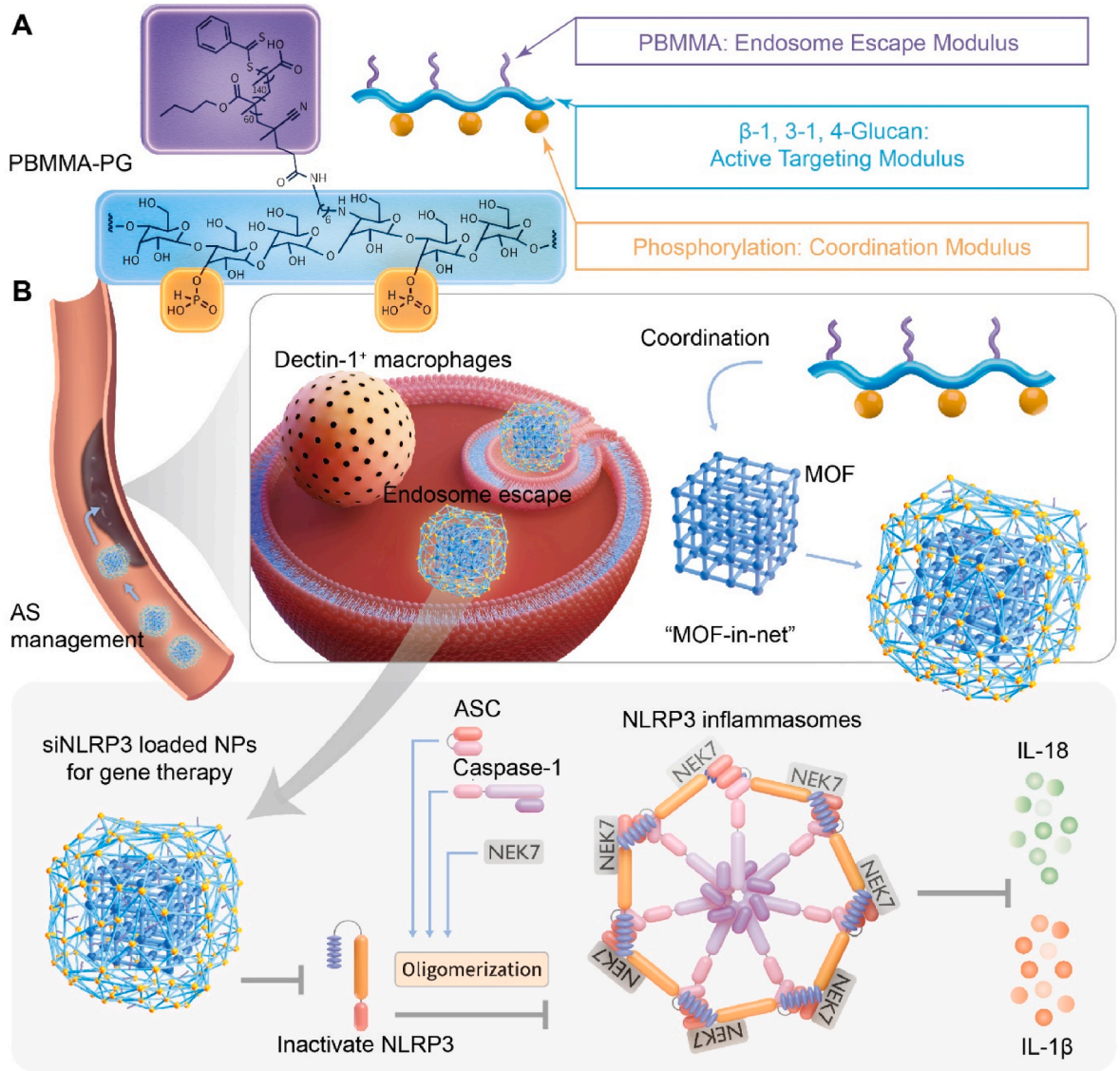

Scheme 1. Conceptual schematic of the nanoparticle fabrication and therapeutic principle underlying its design. (A) The PBMMA-PG is composed by 3 functional modulus, PBMMA branches for endosome escape, β-glucan backbone for active targeting of Dectin-1^{+} macrophages and the phosphorylation modification to facilitate the coordination on MOF cores. **(B)** The hypothetic mechanism of the therapeutic effect caused by the siNLRP3 loaded nanoparticles for AS management. With incorporating a RNAi therapeutic against NLRP3 inflammasome, the maladaptive inflammatory response is resolved via inflammasome neutralization. PBMMA-PG, poly(butyl methacrylate-co-methacrylic acid) branched phosphorylated β-glucan; MOF, metal-organic framework; AS, atherosclerosis; NLRP3, NOD-like receptor family, pyrin domain containing 3; ASC, apoptosis-associated speck-like protein; NEK7, NIMA-Related Kinase 7.

phosphate-containing biopolymers can better protect the MOF from being attacked by biological environments. For example, Fairen-Jimenez et al. reported modifying MOF with phosphorylated polyethylene glycol (PEG), showing advantages in mild modification condition and stable grafting in biological condition [28]. Other researches also suggested the MOF modified with phosphorylated biopolymers remained stable both *in vitro* and *in vivo*, proving the effectiveness of such strategy for biomedical applications [29–32]. However, to advance the application of MOFs in AS genetic theranostics, we need to further develop advanced strategies that give nanoparticles multifunctionalities, tailored to the characteristics of AS and meet the treatment needs. Meanwhile, the strategy should also keep synthesis simple and under mild conditions without toxic reagents, essential for clinical translation of MOFs.

Previous studies indicated the emergence of Dectin-1$^+$ macrophages as hall-marker in AS plaques [33]. Considering the inherent Dectin-1 binding affinity of β-glucan, in this work, a custom-designed multifunctional β-glucan based polymer is synthesized to modify different MOFs for improved AS therapeutic effects. The barley β-1, 3–1, 4-glucan was phosphorylated (PG) to promote the coordination affinity towards iron (III) based MOFs. A pH-sensitive polymeric segment, poly(butyl methacrylate-co-methacrylic acid) (PBMMA), which may alter the hydrophobicity under acidic endosome environment, was conjugated on PG (PBMMA-PG) to further amplify the endosome escape for efficient gene delivery. PBMMA-PG could entrap the MOF in a facile and general coordination binding in mild conditions (Scheme 1). Different iron (III) carboxylate MOFs, including MIL-53 (Fe) and MIL-100 (Fe) were tested as a typical MOF nanoparticle for siRNA loading and reactive oxygen species (ROS) elimination, while their intrinsic T1-weight magnetic resonance (MR) activity may further facilitate the AS diagnosis by MR imaging. As a proof-of-concept, we showed the NOD-like receptor family, pyrin domain containing 3 (NLRP3) counteracted siRNA (siNLRP3) loaded nanosystem could effectively accumulate in AS plaques, resulting a significant plaque reduction. Their macrophages targeting efficiency can further be utilized to enhance the MR signal intensity in artery, indicative a promising theranostic potency. Overall, this study presented a simple, general approach for the design of "all-in-one" nanosystem that synergically achieve RNAi therapeutics and diagnostics, holds great potential for translational applications of MOFs in atherosclerosis.

2. Materials and methods

2.1. Materials

1,4 benzene dicarboxylic acid (H_2BDC), 1,3,5-Benzenetricarboxylic acid (H_3BTC), Iron (III) chloride hexahydrate and 2′,7′-Dichlorofluorescein were purchased from Sigma Aldrich (USA). Quant-it™ RiboGreen RNA Assay Kit and Pierce™ BCA Protein Assay Kit were supplied by Thermo Fisher (USA). The CellTiter-Glo® Luminescent Cell Viability Assay Kit was obtained from Promega Corporation (USA). Cy5-labeled siRNA, NLRP3 siRNA and Scrambled siRNA were purchased from GenePharma (China). The sequences were used as follow: Cy5-labeled siRNA, sense, 5′- UUCUCCGAACGUGUCACGUTT-3'; antisense, 5′- ACGUGACACGUUCGGAGAATT-3'. Scrambled siRNA (siNC), sense, 5′- UUCUCCGAACGUGUCACGUTT-3'; antisense, 5′-ACGUGACACGUUCGGAGAATT-3'. NLRP3 siRNA, sense, 5′- GCUGGAAUCUCUCCACAAUTT; antisense, 5′-AUUGUGGAGAGAUUCCAGCTT-3'. The detailed information of antibodies was listed in Table S1.

2.2. Synthesis of metal organic framework MIL-53 (Fe) and MIL-100 (Fe)

The MIL-53 (Fe) and MIL-100 (Fe) were synthesized via solvothermal method with slight modifications [34,35]. Briefly, 2 mmol of 1,4 benzene dicarboxylic acid (H_2BDC) or 1,3,5-Benzenetricarboxylic acid (H_3BTC) was dissolved in N,N′-dimethylformamide (DMF), 2 mmol of $FeCl_3{\cdot}6H_2O$ dissolved in DMF was then well mixed with organic ligands solution (molar ratio: 1:1) into a final volume of 50 mL DMF, followed by stirring and heated in oil bath at 80 °C overnight. The resulting product was washed with DMF and methanol and heated at 150 °C overnight to remove DMF. The solid was then stirred in a large volume of DI water to remove the traces of DMF.

2.3. Synthesis of PBMMA-PG

The phosphorylated β-glucan polymer (PG) was synthesized as reported elsewhere [36]. Briefly, β-glucan (1 g) was completely dissolved in 100 mL of anhydrous formamide at 70 °C. Following dissolution, 2 mL of triethanolamine (TEA) and 500 mg of polyphosphoric acid (PPA) were introduced into the solution, initiating a 36-h reaction period at 70 °C. The resulting polymer products were precipitated in an equivalent volume of cold ethanol and subjected to overnight dialysis utilizing a membrane with a molecular weight cut-off of 3.5 kDa against Milli-Q water, aimed at eliminating impurities. Subsequently, the final dialysate underwent lyophilization to yield the crude PG polymer (Yield 61.1 %). The poly(butyl methacrylate-co-methacrylic acid) branched phosphorylated β-glucan were synthesized by RAFT polymerization [37]. Briefly, PG (100 mg) was dissolved in DMSO, followed by the addition of methanesulfonyl chloride (MsCl, 2.72 mg), NaI (20 mg) and N-Boc-1, 6-hexanediamine (36 mg) to the solution. The reaction proceeded for 4 h at 75 °C, afterwards, trifluoroacetic acid (TFA) was introduced to remove the BOC groups. PBMMA was synthesized by adding RAFT agent (equivalent to 0. 04 mmol) in 2-propanol, further added methacrylic acid (425 μL, 5 mmol) and butyl methacrylate (304 mg, 2.14 mmol) at the molar ratio of 140:60, followed by the addition of AIBN solution (54 μL, 0.2 M in toluene). The flask underwent nitrogen purging for 40 min after being sealed, followed by immersion in an oil bath at 70 °C for a reaction period of 16 h. Purification of resultant polymer was accomplished with precipitation in cold diethyl ether, followed by separated via centrifugation at 3214×*g* for 5 min. The resulting pellet was then dissolved in methanol and subjected to sequential precipitation in diethyl ether, a process repeated three times to ensure the removal of any remaining unreacted monomers (Yield 33.9 %). The final PBMMA-PG was obtained by dissolving 100 mg aminated PG in 3 mL sodium bicarbonate solution, followed by adding 100 mg of PBMMA in 0.5 mL of DMSO and stirred for overnight. After the conjugation to get PBMMA-PG, the final product was dialyzed against Milli-Q water and characterized by ^{1}H NMR (Yield 44.6 %).

2.4. Nanoparticles characterization

The hydrodynamic size, polydispersity index and zeta (ζ)-potential of nanoparticles were characterized using dynamic light scattering (DLS) analysis. Samples were recorded in aqueous solution by a Malvern Zetasizer NanoZS instrument at 25 °C, measurements were performed three times with 11 subruns for each sample. Transmission electron microscopy (TEM) and scanning electron microscopy (SEM) imaging were performed to visualize the morphology and homogeneity of the prepared nanoparticles. For TEM analysis, samples were drop-casted on a Formvar/Carbon 200 Mesh, copper grid (Electron Microscopy Sciences, FCF200-Cu-50), the micrographs were collected on a TalosF200i with an acceleration voltage of 200 kV. The samples for SEM tests were coated with carbon and imaged using Supra 55 Scanning Electron Microscope (Zeiss). Fourier Transform Infrared Spectroscopy (FTIR Spectroscopy) was performed to identify the chemical properties of the nanoparticles, FTIR was carried out using a Cary 600 Series Spectrometer (Agilent). The phase identification of MOF NPs was accomplished by Powder X-ray diffraction (PXRD) analysis. MOF phase identification was carried out using Bruker D8 Advance X-Ray diffractometer, with Cu-Kα radiation (1.5418 Å) at 40 kV over the range from 5° to 50 in 0.0102 steps.

2.5. siRNA nanoparticles preparation

The siRNA stock solution was prepared according to the manufacturer's instruction. Briefly, 200 pmol si-NC/si-NLRP3 (20 μL of stock solution) was mixed with 26 μg MIL-53 (stock solution in ethanol), followed by added to 100 μL DEPC H_2O. The PBMMA-PG solution was prepared in DEPC H_2O, 26 μg of PGMMA-PG in 100 μL DEPC H_2O was subsequently added dropwise to the solution containing siRNA and MIL-53, the NPs were formed by mixing at RT for 150 min, the total volume is around 250 μL.

2.6. Molecular dynamics (MD) simulation

The construction of polymer chains and small molecules were conducted in ChemDraw (CambridgeSoft, U.S.). All molecular structures were assembled, and force fields generated using the Sobtop [38]. Individual phosphorylated β-1,3–1,4-glucans chain (PG) was composed of six glucose monomers, and two glucose monomers were phosphorylated at the second and third carbon position in each chain. The PBMMA copolymer was composed by 3 butyl methacrylate unit and 7 methacrylic acid unit, based on the actual ratio between butyl methacrylate and methacrylic acid, as shown in Fig. S2. Total charge of each PBMMA-PG chain under different pH condition was calculated by OpenBable [39]. The initial simulation box size was 5 nm in each dimension (x, y, and z). One PBMMA-PG chain was randomly placed into the simulation box, based on the actual experimental protocols, after which the system was solvated. Simulation parameters were optimized as followings. The constructed system was simulated utilizing the AMBER force field and the GROMACS simulations package v. 2021.5. The simulations were carried out using an isothermal-isobaric ensemble (constant NPT). The system composed of PBMMA-PG was annealed in temperatures of 0–298 K for 4 cycles with in total 1 ns to minimize the energy of the whole system, followed by a 10 ns simulation at the temperature of 298 K to study polymers' behavior and acquire an atomistic insight on the experimental systems. The systems were considered to have reached equilibrium by observing the results for hydrogen bond numbers and the number of close contacts as a function of simulation time. The portion of the simulation trajectory was used for analysis.

Hydrogen bonds, and number of contacts were determined using the gmx hbond and gmx mindist tools, respectively, that are provided with the GROMACS package. The default hydrogen bond parameters were used in calculating the number of hydrogen bonds formed in different cases. The distance cut-off for the number of contacts was set at 0.6 nm. The average of these averages was calculated and used in the determination of standard deviation. The Visual Molecular Dynamics (VMD) program was used to visualize and render the figures.

To evaluate the surface tension of the system, after the aforementioned 10 ns of simulation, a bi-phase simulation cell was constructed by expanding the z-axis of original simulation box into 10 nm. The simulations were carried out using an isothermal-isobaric ensemble (constant NPT). The system was annealed in temperatures from 0 to 298 K for 4 cycles with in total 1 ns to minimize the energy of the whole system, followed by an extra 1 ns simulation at the temperature of 298 K to study polymers' behavior. Afterwards, the pressure in different direction (xx, yy and zz) were determined using the gmx energy tools, which is provided with the GROMACS package. Calculation of an average dynamic surface tension in the water/gas interface was based on Eq. (1).

$$\gamma = \lim_{\tau \to \infty} \frac{1}{\tau} \int_0^{\tau} \gamma(t) dt \tag{1}$$

where, γ represents the surface tension and τ represents the time.

2.7. RiboGreen assay

The RiboGreen assay was conducted to quantify the concentration of siRNA payloads encapsulated in the as-synthesize NPs. Briefly, after the preparation of siRNA-loaded GAMMA-53 and GAMMA-100 NPs, a mild acidic buffer solution (pH 5.0) was used to collapse the MOF NPs as described previously [40]. The RNA standard curve for the quantification was prepared according to the manufacturer's instructions. The measurement was accomplished using a fluorescence microplate reader and standard fluorescein wavelengths (excitation 480 nm, emission 520 nm).

2.8. Cells and cell culturing

The human monocytes THP-1 cell line (Cat# TIB-202) and murine macrophages RAW 264.7 cell line (Cat# TIB-71) purchased from the American Type Culture Collection (ATCC) were maintained in RPMI 1640 medium or Dulbecco's modified Eagle's medium (DMEM) supplemented with 10 % fetal bovine serum (FBS, v/v), 100 U/ml penicillin and streptomycin. Cells were maintained in a humidified atmosphere of 5 % CO_2 at 37 °C.

2.9. Quantification of cellular reactive oxygen species (ROS)

To assess cellular ROS levels, RAW 264.7 cells were seeded at 3×10^5 cells per well in a 6-well dark plate for 24 h. The cells were then stimulated with Lipopolysaccharide (LPS, 1 μg/mL) for 6 h to induce the overproduction of ROS. Afterwards, cells were treated with GAMMA-53 NPs for 24 h at a concentration of 250 μg/mL, followed with incubating with DCFDA probe for further analysis.

2.10. Cell viability

The cytotoxicity of different nanomaterials was evaluated by using the CellTiter-Glo® Luminescent Cell Viability Assay Kit, according to the manufacturer's instructions. Briefly, indicated cells were cultured and seeded into opaque-walled 96-well plates at a density of 1×10^4 cells per well. 24 h later, different groups were added at the indicated concentrations and incubated for extra 48 h. Afterwards, cells were allowed to equilibrate at room temperature for approximately 30 min before adding the celltiter glo reagent. A volume of 100 μl of the CellTiter-Glo® Reagent was then added to 100 μl medium containing cells in the 96-well plates, followed by mixing for 2 min to induce cell lysis. The luminescence was obtained in a multimode microplate reader (Tecan Trading AG, Switzerland).

2.11. Inflammasome stimulation

The stimulation of NLRP3 inflammasome was accomplished by following a well-established procedure reported elsewhere [41]. Briefly, THP-1 cells were incubated with RPMI-1640 containing 150 nM or 100 ng/mL of phorbol 12-myristate 13-acetate (PMA) for 24 h to obtain macrophages. Afterwards, for NLRP3 activation, macrophages were primed with LPS (50 ng/mL) for 3 h, followed by the addition of nigericin (10 μM) in serum-free medium for 60 min.

2.12. Flow cytometry analysis

The cellular uptake of nanoparticles was evaluated by flow cytometry. Briefly, GAMMA-53 and GAMMA-100 NPs were labeled by fluorescein isothiocyanate (FITC) for fluorescent imaging purpose. Cells were proceeded in 6-well plates at the density of 3×10^5 cells per well. 24 h later, cells were incubated with FITC-GAMMA-53 or FITC-GAMMA-100 at the concentration of 0.2 mg/mL 4 h after incubation, cells were collected to prepare single-cell suspension. After washing with pre-cold PBS to remove debris and culture media, cells were incubated with

blocking buffer to block non-specific binding sites, followed by staining with PE-conjugated Dectin-1 antibody. Subsequently, cells were washed with washing buffer (PBS with 1 % bovine serum albumin) to remove unbound antibodies and blocking reagents. Data was acquired on BD LSRFortessa™ X-20 flow cytometer and analyzed using FlowJo software.

2.13. Western blotting assay

Cells pretreated with different formulations were detached by scraper and lysed with cold RIPA buffer, followed by fully lysed in a FS30D bath sonicator (Theromo Fisher, USA). The total proteins were extracted and quantified using BCA assay (Thermo Fisher, USA). For western blotting analysis, proteins were denatured and separated using a 4–12 % SDS-Polyacrylamide gel electrophoresis. Subsequently, the proteins were transferred onto a polyvinylidene fluoride (PVDF) membrane, which had been pre-activated with methanol. Following a 5-min blocking step with EveryBlot Blocking buffer (Bio-Rad), the membranes were then incubated overnight at 4 °C with primary antibodies that had been appropriately diluted. On the second day, following three washes with 1 × TBST, the membranes underwent additional incubation with corresponding secondary antibodies for 1 h at room temperature. Immunoblot signals were subsequently detected using Clarity™ Western ECL Substrate (Bio-Rad) and analyzed utilizing ImageJ software. The corresponding information of antibodies were listed in Table S1.

2.14. Animals

Six-to eight-week-old male apolipoprotein E-deficient ($ApoE^{-/-}$) C57BL/6 mice were purchased from the Jackson laboratory (Bar Harbor, ME). After acclimatization for 7 days, mice were fed with high-fat western diet (WD) for 14 weeks to construct atherosclerotic murine model. All procedures were conducted in accordance with protocols approved by the Institutional Animal Care and Use Committee at School of Basic Medical Sciences of Zhejiang University (SYXK(zhe) 2019–0011).

2.15. In vivo toxicity evaluation

Healthy mice (male, six-to eight-week-old) were intravenously (i.v.) injected with 150 μL NPs containing 2.1 mg/kg GAMMA-53, the same volume of PBS was i.v. injected as control group. Forty-eight hours post-injection, mice were euthanized and the major organs, including heart, liver, spleen, lung and kidney were harvested and stained with hematoxylin and Eosin (H&E) for histology study.

2.16. In vivo magnetic resonance imaging (MRI)

In vivo MRI tests were performed on a 7T Bruker Biospec System equipped with a gradient system capable of 660 mT/m maximum strength and 110-μs rise time. $ApoE^{-/-}$ mice with 14 weeks WD fed were intravenously injected with PBS or GAMMA-53 NPs (4 mg/mL, 200 μL). MRI was performed at 3 time points: pre-contrast, 6 h post-contrast and 24 h post-contrast. A 3D gradient echo T1-weighted sequence was performed before (pre-contrast) and after (post-contrast) contrast agent injection. The normalized enhancement ratio (NER) was calculated to quantify the enhancement level in MRI images, as the formula is $NER = \frac{(SI_{post} - SI_{pre})}{SI_{pre}}$. The SI_{pre} and SI_{post} refers to the signal intensity pre or post injection with contrast.

2.17. Therapeutic studies of GAMMA-53 NPs

After 8 weeks of WD feeding, $ApoE^{-/-}$ mice were randomly divided into 3 groups, n = 10 each group: (1) PBS or (2) GAMMA-53-siNC or (3) GAMMA-53-siNLRP3 was intravenously (i.v.) injected twice a week for another 6 weeks, while being maintained on the WD. Afterwards, all mice were euthanized and perfused with PBS and 4 % paraformaldehyde. The serum was collected for the detection of IL-1β and IL-18 cytokine secretion in different groups. The whole aorta was harvested and stained with Oil Red O (ORO). Furthermore, the 8 μm thick cryosections of the aortic root were prepared. These cryosections were further stained with ORO and Masson's trichrome. In addition, the cryosections of the aortic root were stained with antibodies, including Dectin-1 and NLRP3, respectively, for immunohistochemistry analysis. Finally, the atherosclerotic plaque areas, lesions and positively stained areas were determined by Image J (Version 1.54).

2.18. Statistical analysis

All experiments were conducted in triplicate unless otherwise noted. Data are presented as mean ± standard deviation. Statistical analyses were performed using GraphPad Prism 9.5.1 software. Student's *t*-test (two-tailed) was utilized to analyze data within two groups, while one-way analysis of variance (ANOVA) with Fisher's least significant difference post hoc analysis was employed to compare three or more groups. A p-value <0.05 was considered statistically significant, denoted as $^*p < 0.05$, $^{**}p < 0.01$, and $^{***}p < 0.001$.

3. Results and discussion

3.1. Design and preparation of iron-based MOFs

We first determined to synthesize typical MOFs with different topologies and array of metal-ligand combinations. It has been reported that among all the metals used in MOFs, iron is one of the least toxic [42]. In combination with its inherent T1-weight MR activity, we chose iron-based MOF in the current study. The organic ligands with varying quantities of carboxyl groups, including terephthalic acid (H_2BDC) and 1,3,5-benzenetricarboxylic acid (H_3BTC), were chosen for tailored cooperation with iron metal salts. The schematic illustration for the NPs' preparation is shown in Fig. 1A. Briefly, two representative Fe(III)-MOFs with distinct morphology, MIL-53 (Fe) and MIL-100 (Fe), were synthesized [11]. Dynamic light scattering (DLS) and phase analysis light scattering (PALS) measurements indicated the particle size along with surface charge, in which MIL-53 (Fe) was 120.6 nm with +32.5 mV, MIL-100 (Fe) was 111.6 nm with −9.6 mV (Fig. 1B–C). Fourier-transform infrared (FTIR) spectra was acquired using KBr pellets, the peaks characteristic for the symmetric and asymmetric stretching vibrations of C–O pertaining to the carboxylate groups at 1524 cm^{-1} and 1380 cm^{-1} confirmed the presence of ligand, and the peak at 863 cm^{-1} referred to the δ (OH) modes of the bridging hydroxyl group (Fe–O(H)–Fe, Fig. 1D) [43]. The phase identification of both MIL-53 (Fe) and MIL-100 (Fe) was confirmed via Powder X-ray diffraction (PXRD). The experimental diffractograms shown in Fig. 1E matched the patterns simulated from the single-crystal structures, with the typical peak broadening resulting from the nano-size of the particles. Transmission electron microscopy (TEM) and scanning electron microscopy (SEM) images showed that both MOF NPs displayed monodispersed morphology and crystalline structure (Fig. 1F–**G,** and Fig. S1). Specifically, MIL-53 (Fe) showed a hexagonal bipyramidal shape, whereas MIL-100 (Fe) was round with a less defined morphology.

3.2. Multifunctional PBMMA-PG could modify MIL-53 (Fe) and MIL-100 (Fe) through coordination bonding

The as-synthesized MOF NPs may fall short for AS genetic therapy due to their limitation in colloidal stability, biocompatibility, and plaque accumulation, therefore they need an additional surface functionalization [28,44]. Previous studies proposed the modification of the exterior surface of MOF particles via coordination bonds, showing advantages in simple modification schemes, mild reaction conditions and

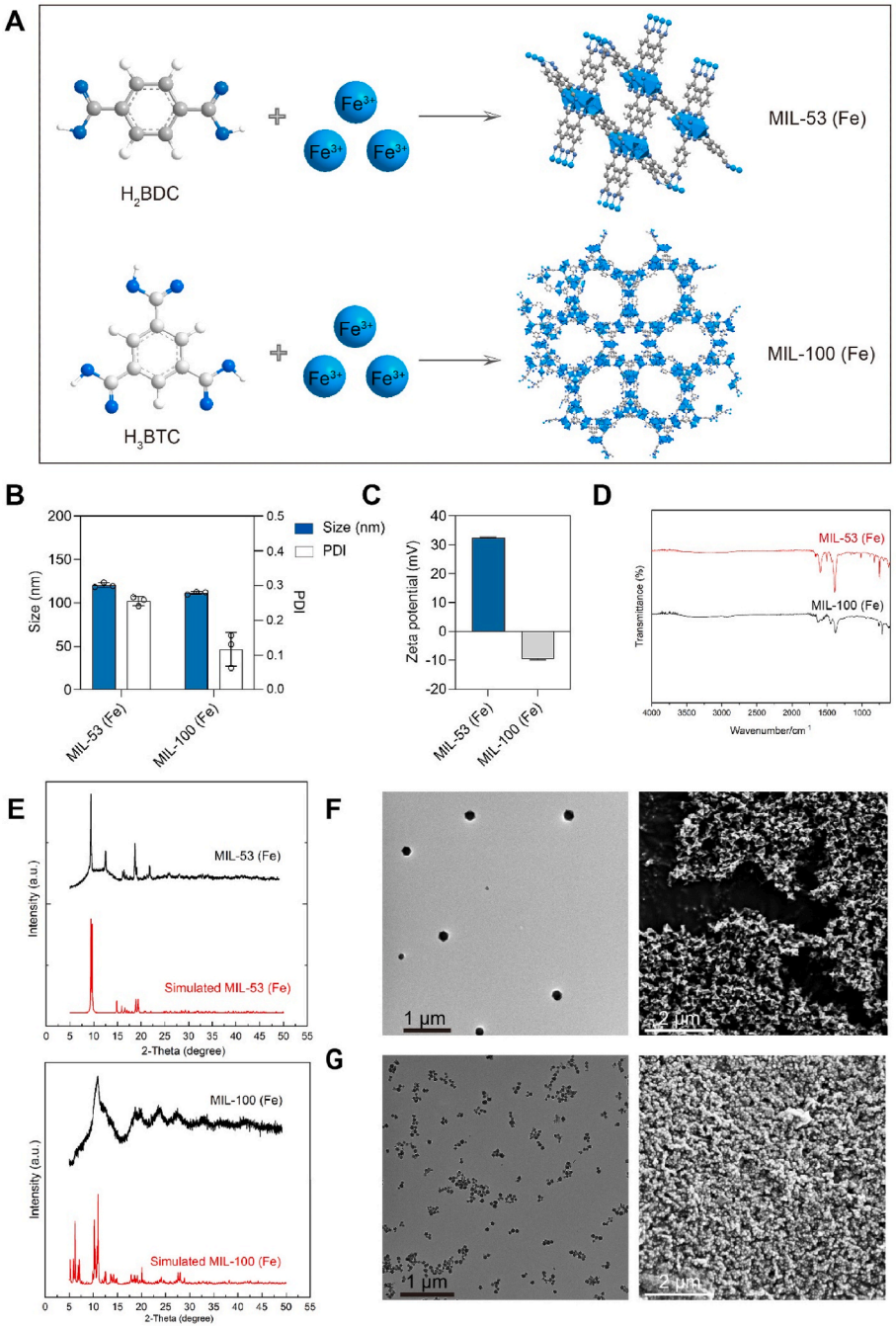

Fig. 1. Preparation and characterization of iron-based MOF NPs. (A) Schematic illustration of the preparation of MIL-53 (Fe) and MIL-100 (Fe) NPs. The crystal structure was predicted and visualized by Mercury 4.0 (CCDC cif: 640536; 2088536). **(B)** Size and **(C)** zeta-potential of iron-based MOF NPs was determined using DLS and PALS analysis. **(D)** FTIR Spectroscopy showed the chemical properties of the synthesized MIL-53 (Fe) and MIL-100 (Fe) NPs. **(E)** PXRD analysis was performed to characterize the crystalline structures of iron-based MOF NPs. TEM and SEM images of **(F)** MIL-53 (Fe) NPs and **(G)** MIL-100 (Fe) NPs. Data is shown as mean ± SD.

tailored functionalization degrees [28,45,46]. Upon such consideration, we formulated a capping agent for functionalizing MOFs, tailored to meet the specific needs of AS treatment. Previous study noted a distinctive expression of Dectin-1 on macrophages in atherosclerotic lesions [47], suggesting that employing β-glucan, a recognized Dectin-1 ligand, can provide targeting capacity towards atherosclerotic macrophages. Thus, we designed and synthesized PBMMA-PG (see **Methods** and Fig. S2 for synthesis details and ^{1}H NMR characterization) with three distinct functional modulus: β-glucan backbone to impart the polymer with atherosclerotic Dectin-1^{+} macrophages selectivity; phosphates groups to coordinate with metal centers to immobilize the polymer onto host MOF NP and PBMMA branches to endow the polymer with pH-dependent morphology alteration to facilitate the endosome escape (Fig. 2A) [48].

Initially, we investigated the efficacy of PBMMA-PG in modifying iron-based MOFs. Following a previously established protocol [28], surface functionalization with PBMMA-PG on MIL-53 (Fe) or MIL-100 (Fe) was achieved by incubating PBMMA-PG with each MOF at a 1:1 wt ratio in aqueous solution for 2 h. Following the post-modification process, the obtained nanohybrids were separately denoted as PBMMA-PG Anchored MIL-53 (Fe) MOF Assembly (GAMMA-53) or PBMMA-PG Anchored MIL-100 (Fe) MOF Assembly (GAMMA-100). DLS

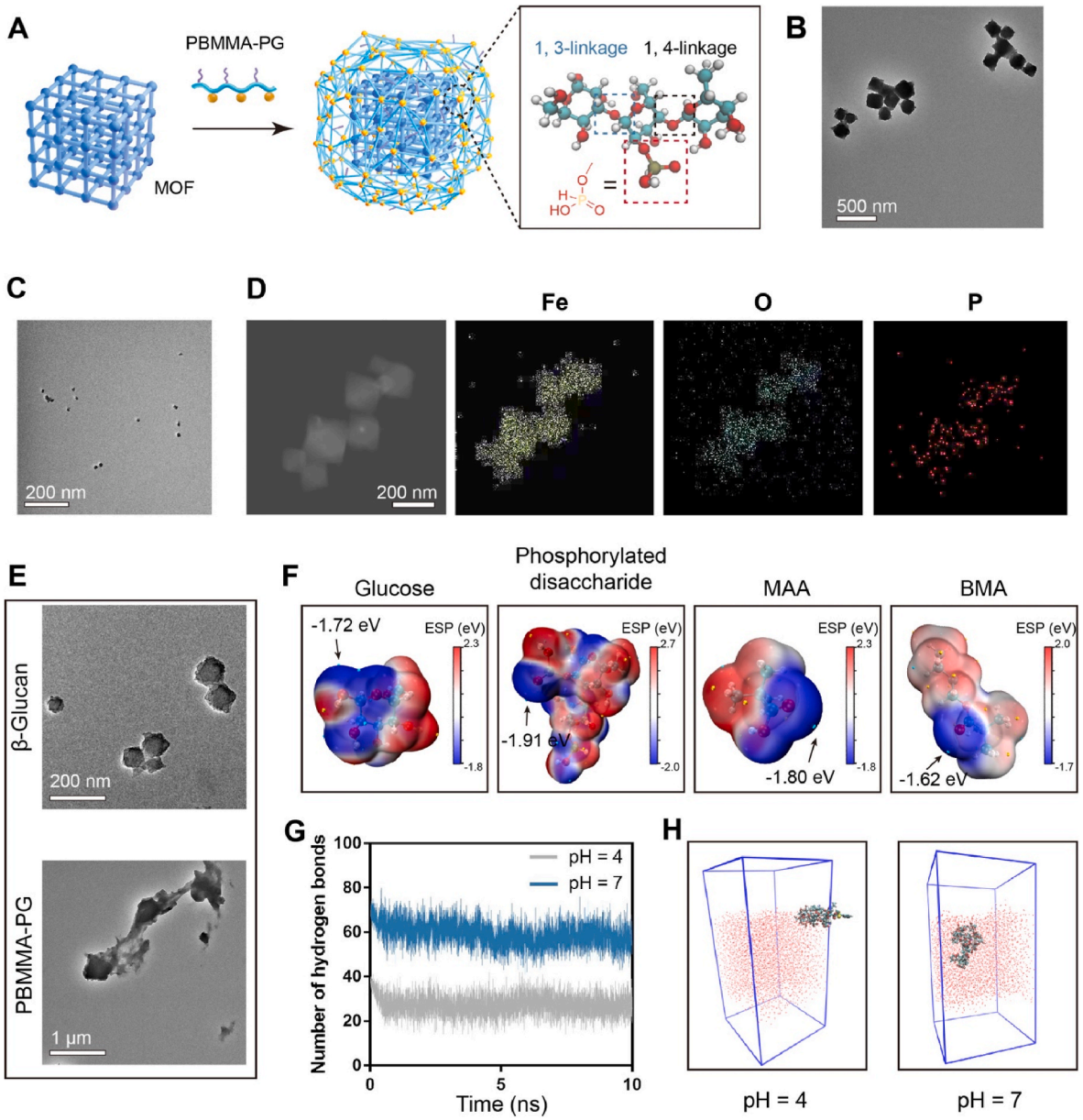

Fig. 2. Post-coordination of multifunctional PBMMA-PG on MOF NPs. (A) Schematic illustration of post-modification of PBMMA-PG on MOF NPs, and the hypothetic coordination binding site. **(B)** TEM images of GAMMA-53 NPs and **(C)** GAMMA-100 NPs. **(D)** Elemental mapping analysis was performed to identify the Fe and P elements within the GAMMA-53 NPs. **(E)** TEM images of MIL-53 (Fe) incubating with excess amount of PBMMA-PG or β-glucan under the polymer/MOF ratio of 4:1 (w/w). **(F)** Electrostatic potentials (ESP) distribution of different molecules and their corresponding extreme points at the molecular van der Waals surface. The regional maximum and minimum ESP point is separately illustrated as golden and cyan sphere, and the minimum ESP value for each molecule is indicated by arrow. **(H)** Number of formed hydrogen bonds between PBMMA-PG and water across the simulation time of 10 ns. **(G)** Snapshot analysis of PBMMA-PG configurations in a water/gas biphase cell under different pH conditions after 1 ns of annealing to find the optimal configuration. Water molecules were represented as red dots, whereas the PBMMA-PG molecule was illustrated in Corey-Pauling-Koltun (CPK) style.

measurements revealed minimal changes in size and PDI following PBMMA-PG modification of the MIL-53 (Fe) or MIL-100 (Fe) (Fig. S3A and Table S2). Consistently, TEM images demonstrated a well-preserved morphology and monodispersity of GAMMA-53 and GAMMA-100 comparing to their parent MOFs (Fig. 2B–C and Figs. S3B–C). We further conducted elemental mapping analysis in scanning TEM, which showed a random distribution of Fe and P elements within post-modified NPs, confirming the successful grafting of PBMMA-PG (Fig. 2D). Increasing the degree of PBMMA-PG modification impacted the crystalline structure of the MOF. When increasing the PBMMA-PG/MOF ratio from 1:1 to 4:1, a clear collapse of MOF crystalline structure was observed, whereas this was not observed in incubating MOF with excess unphosphorylated β-glucan under the same condition (Fig. 2E). This can be ascribed to the strong and fast coordination between phosphonates and metal ions, which make it challenging to order them on the longer length scales needed to generate crystalline materials [31,49]. To further elucidate the phosphonates assisted MOF coordination, we adopted a quantum chemistry method to interpret the electrostatic potential (ESP) of different representative segments in PBMMA-PG, including glucose unit, phosphorylated disaccharide (composed by 1, 3- and 1, 4-linked glucoses), butyl methacrylate (BMA) and methacrylic acid (MAA). The calculations of all molecular structures were carried out using the Gaussian 09 package [50]. The geometrical optimization and electrostatic potential were performed to obtain more accurate electronic structure information by the B3LYP functional with diffuse function basis set 6-311+G (d, p) [51,52], and the electrostatic potential

of each molecule was analyzed by Multiwfn [53]. As shown in Fig. 2F, the molecular surface with the lowest ESP was observed in the phosphate groups modified on the 2-OH of the glucose residues (−1.91 eV), which is lower than that from the hydroxyl groups from unmodified glucose (minimum −1.72 eV from 1-OH), phosphate groups modified on the 3-OH of the glucose residue (−1.44 eV) and the carboxyl group from MAA (−1.80 eV), indicative of the potential primary coordination site towards iron centers.

Another important functional modulus from PBMMA-PG is derived from the PBMMA induced endosome escape capability. Previous work has shown that copolymer with a MAA: BMA molar ratio of 140:60 exhibited superior endosomal escape properties [48,54]. To further elaborate the potential mechanism beneath the phenomenon, we adopted molecular dynamics (MD) simulation to elaborate the molecular behavior of PBMMA-PG under different pH condition in aqueous solution. The protonation status of PBMMA-PG in different pH condition was calculated by OpenBabel [39]. Their corresponding topology files were sequentially generated by Sobtop and further subjected to GROMACS for 10 ns simulation [38,55]. Final snapshot after MD simulations demonstrated that PBMMA-PG, when dispersed in a neutral aqueous solution (pH 7), showed a more extended conformation in water compared to its configuration in an acidic environment (pH 4), partly indicating the acidic-induced hydrophobicity alteration of PBMMA-PG (Fig. S4A). This is further confirmed by calculating the number of formed hydrogen bonds and close contacts between PBMMA-PG and water, which showed a substantially reduced contact between PBMMA-PG with water under acidic condition (Fig. 2G, Fig. S4B). Moreover, we compared the surface tension (γ) of PBMMA-PG containing aqueous solution under different pH value in a 3D gas-water bi-phase simulation cell (**Methods**) [56]. Consistently, after the annealing process (1 ns), the preferred configuration for PBMMA-PG under neutral condition was stretched and resided in water, whereas under acidic condition, PBMMA-PG was prone to aggregate in the interface (Fig. 2H). This is also confirmed as the average surface tension (followed by 2 ns extra simulation after annealing) of acidic PBMMA-PG solution is substantially higher than that under neutral pH value (Fig. S4). Therefore, the mechanism of PBMMA induced endosome escape is potentially attributed from its pH-responsive morphological changes to increase hydrophobicity of the copolymer under acidic conditions, thereby disrupting the integrity of the endosome membrane [7].

3.3. *GAMMA-53 exhibited higher gene silencing efficacy on Dectin-1$^+$ macrophages*

Despite GAMMA-53 and GAMMA-100 share the same surface-modification scheme, we next investigated whether variations in MOF cores might influence biological performance of the nanohybrids for gene delivery. Considering the Dectin-1 targeting capability from PBMMA-PG, we first evaluated the uptake of GAMMA-53 and GAMMA-100 by Dectin-1$^+$ human THP-1 macrophages through flow cytometry analysis [57]. Fluorescein isothiocyanate (FITC) was conjugated on the polymer backbone in a previously established protocol [48], and the gating strategy is shown in Fig. S5. As shown in Fig. 3A–C, after 4 h of incubation, THP-1 derived macrophages treated with GAMMA-53 exhibited a substantially higher FITC$^+$ proportion compared to those treated with GAMMA-100 (31.4 ± 7.1 % *vs.* 15.7 ± 2.7 %, $p < 0.05$), indicating a potential impact of MOF cores on cellular uptake of the nanohybrids. As another critical aspect for achieving efficient gene silencing, the encapsulation efficiency (EE%) of siRNA in GAMMA-53

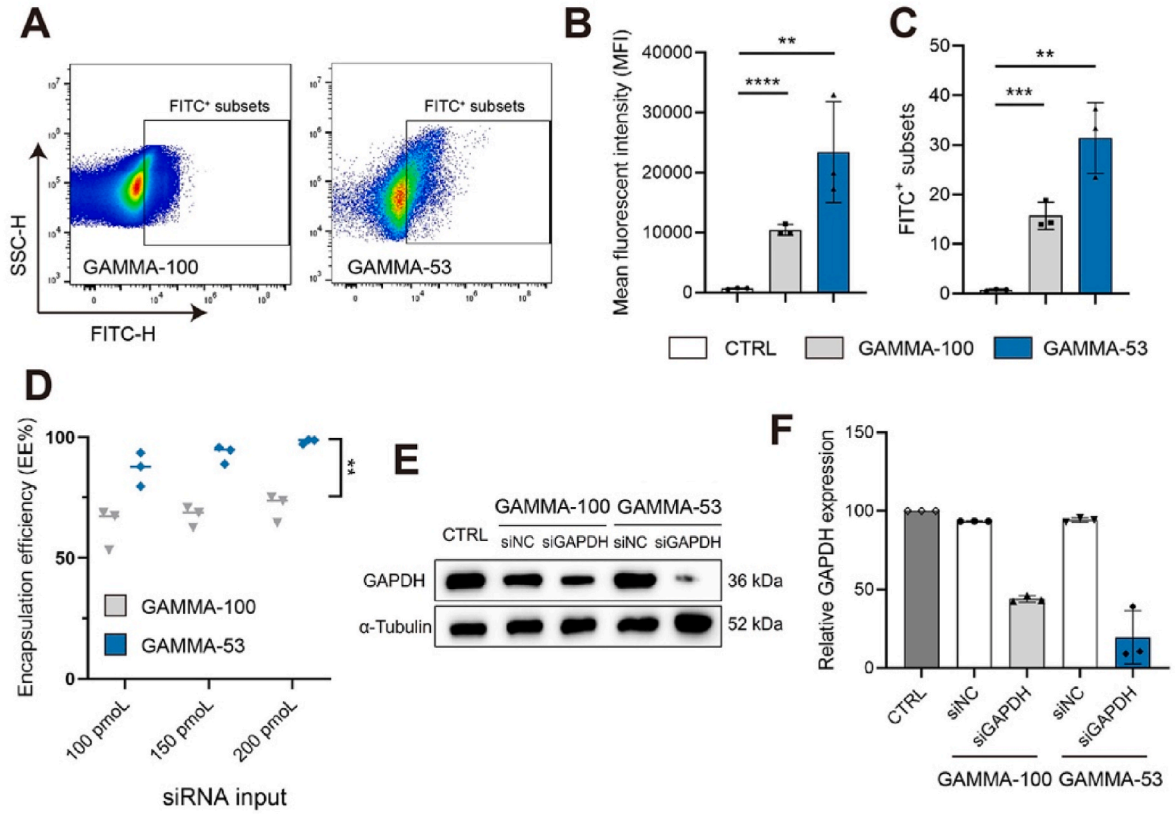

Fig. 3. *In vitro* comparison of GAMMA-53 and GAMMA-100 on gene silencing capacity. (A) Cellular uptake of GAMMA-53 and GAMMA-100 in THP-1 cells were determined by flow cytometry analysis, and the **(B)** quantitative evaluation on mean fluorescence intensity (MFI) as well as **(C)** positive cells percentage confirmed the enhanced cellular uptake of GAMMA-53. **(D)** RiboGreen assay was performed to identify the siRNA encapsulation efficiency of GAMMA-53 and GAMMA-100. **(E)** and **(F)** Western blotting analysis of the expression of GAPDH and α-Tubulin after the treatment of siGAPDH loaded GAMMA-53 and GAMMA-100. Data is presented as mean ± SD. **, $p < 0.01$; ***, $p < 0.001$; ****, $p < 0.0001$.

and GAMMA-100 were tested by RiboGreen assay (Fig. 3D). The EE% of siRNA in both nanohybrids were positively correlated with siRNA input. Notably, with a fixed NPs concentration at 0.2 mg/mL, across siRNA input amount ranging from 100 pmol to 200 pmol, the EE% from GAMMA-53 were pervasively higher than that from GAMMA-100, indicating a superior siRNA encapsulation efficacy from MIL-53 (Fe).

To further access the gene silencing efficacy of different nanohybrids, GAMMA-53 and GAMMA-100 encapsulating siGAPDH or scrambled siRNA (siNC) at the siRNA concentration of 100 nM were incubated with THP-1 macrophages for 48 h, and gene silencing efficacy were determined by western blotting analysis (Fig. 3E–**F**) [58,59]. The results demonstrated that under the same siRNA concentration, GAMMA-53 mediated a statistically significant increase in the gene silencing capacity, achieving an 80.4 % reduction in target protein (GAPDH) expression. In contrast, the knockdown efficiency was merely 56.0 % in the GAMMA-100. Considering the superior behavior of GAMMA-53, we then exploited its storage stability, which is crucial for the potential clinical translation. Consequently, stability of GAMMA-53 was maintained after five days of storage at 4 °C, as confirmed by TEM analysis. (Fig. S6A). Besides of the storage of NPs in aqueous solution, the produced GAMMA-53 can be lyophilized and feasibly redispersed in water. The re-dispersed GAMMA-53 still preserved their integrity and dispersity, signifying the colloidal stability upon PBMMA-PG modification. (Fig. S6B).

Altogether, the *in vitro* results demonstrate that GAMMA-53 exhibited superior properties as gene delivery vehicle, in terms of enhanced cellular uptake, efficient EE% and superior gene silencing capacity. Therefore, the GAMMA-53 was used for the following studies.

3.4. GAMMA-53 exhibited metallic nanozymatic property for reactive oxygen species (ROS) scavenging

Iron based MOFs have been reported to possess intrinsic properties as nanozyme, presenting peroxidase-like catalytic activity towards excessive reactive oxygen species (ROS) production [60]. Given the pervasive overproduction of ROS observed in AS plaques and their potential role in AS progression, we hypothesize that the ROS scavenging capability of GAMMA-53 could enhance its therapeutic potential for AS treatment. We first proceeded to examine the potential ROS neutralization capability of GAMMA-53 *in vitro*, as reflected by the fluorescence intensity of 2′,7′-dichlorofluorescin diacetate (DCFDA) [61]. After treatment with lipopolysaccharides (LPS, 1 μg/mL) for 6 h, a pronounced ROS production was observed in RAW 264.7 macrophages (Fig. 4A). In contrast, when the macrophages were co-incubated with GAMMA-53 NPs at the concentration of 250 μg/mL, a marked decrease (61.0 %) in fluorescence intensity was observed, indicating its potent antioxidative activity. Subsequently, a more detailed antioxidant efficacy from GAMMA-53 were quantified by flow cytometry analysis. Co-incubation of GAMMA-53 at 250 μg/mL reduced the proportion of $DCFDA^+$ cells from 22.7 % to 4.7 %, and a 46.0 % reduction in mean fluorescence intensity (Fig. 4B–D). These findings collectively confirmed the inherent function of the designed GAMMA-53 with metallic nanozyme property for ROS scavenging.

3.5. Inflammation resolution via targeting of NLRP3 inflammasome

Having confirmed the potency of GAMMA-53 as gene delivery vehicle, we then sought to identify the proper therapeutic target to achieve the envisioned AS treatment. Previous clinical trials validated the effectiveness of targeting IL-1β, which is mainly derived by NLRP3 inflammasomes activation, in mediating AS progression [62]. Nonetheless, the systematic intervention of IL-1β was also associated with higher chance of adverse events such as pneumonia [63]. Therefore, cellular targeted anti-IL-1β therapy has been hypothesized to be preferable to systemic treatments to avoid the aforementioned complications [9]. Thus, we further investigated whether the GAMMA-53, with

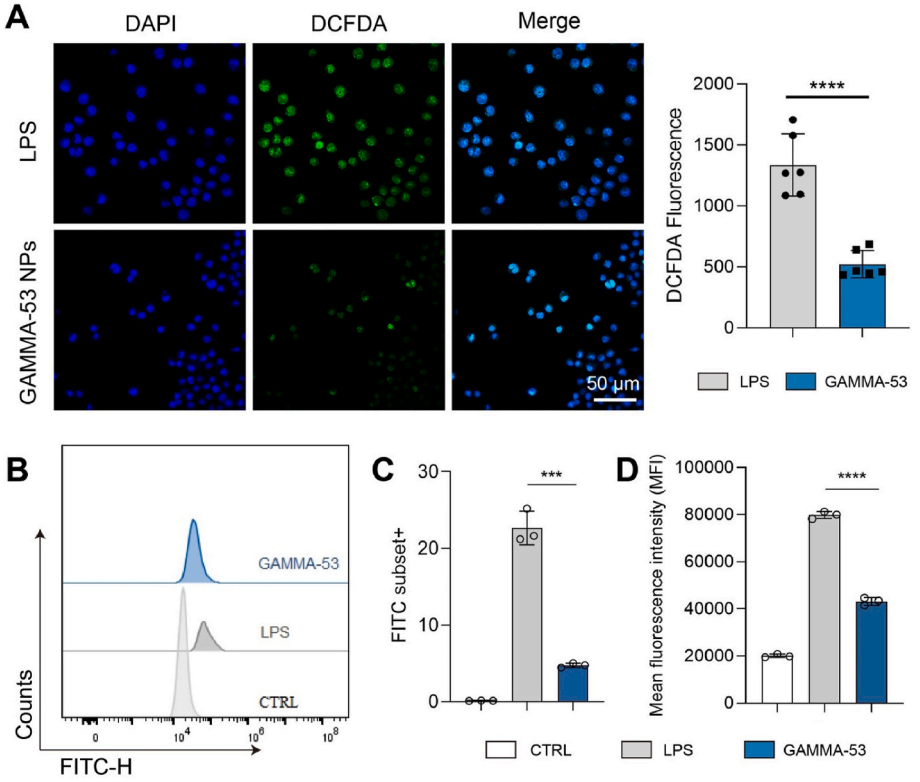

Fig. 4. Identification of GAMMA-53 NPs as intrinsic ROS scavenger. (A) DCFDA fluorescence was determined by confocal imaging after treatment with GAMMA-53 NPs. **(B–D)** Flow cytometry analysis was performed to explore the fluorescent intensity of DCFDA in different groups. Data is presented as mean ± SD. ***, $p < 0.001$; ****, $p < 0.0001$.

encapsulating the NLRP3 counteracted siRNA (siNLRP3), could or not regulate the aberrant production of IL-1β. We first checked the biocompatibility of GAMMA-53 on murine macrophages RAW 264.7 and murine cardiac myoblast H9C2 cells. As shown in Fig. S7, after 48 h of incubation, RAW 264.7 cells showed statistically significant cytotoxicity (viability <60 %) at MIL-53 (Fe) concentrations exceeding 100 μg/mL, whereas for H9C2 cells, this threshold was observed at 250 μg/mL. In contrast, GAMMA-53 exhibited no cytotoxicity up to MIL-53 (Fe) concentrations of 500 μg/mL, suggesting that surface modification with PBMMA-PG mitigated the cytotoxic effects associated with the native MIL-53 (Fe) NPs.

After confirming the *in vitro* biocompatibility, to further track the cellular uptake process of siRNA residing in GAMMA-53, the red fluorescence dye cyanine 5 NHS ester (Cy5) was labeled on siRNA (Cy5-siRNA) and encapsulated within GAMMA-53. As shown in Fig. 5A, a significant red fluorescence was exclusively detected in THP-1 macrophages after 6 h incubation with GAMMA-53/Cy5-siRNA containing 50 nM of siRNA, whereas the fluorescence is not observed in pristine Cy5-siRNA, indicating a robust siRNA uptake and sequential endosome escape upon entering the cells. Moreover, the corresponding statistical analysis further strengthened the efficient endosomal escape capability mediated by GAMMA-53, with an average intensity of 62.08 a.u. (Fig. S8).

Next, we tested GAMMA-53 as siRNA delivery system for the

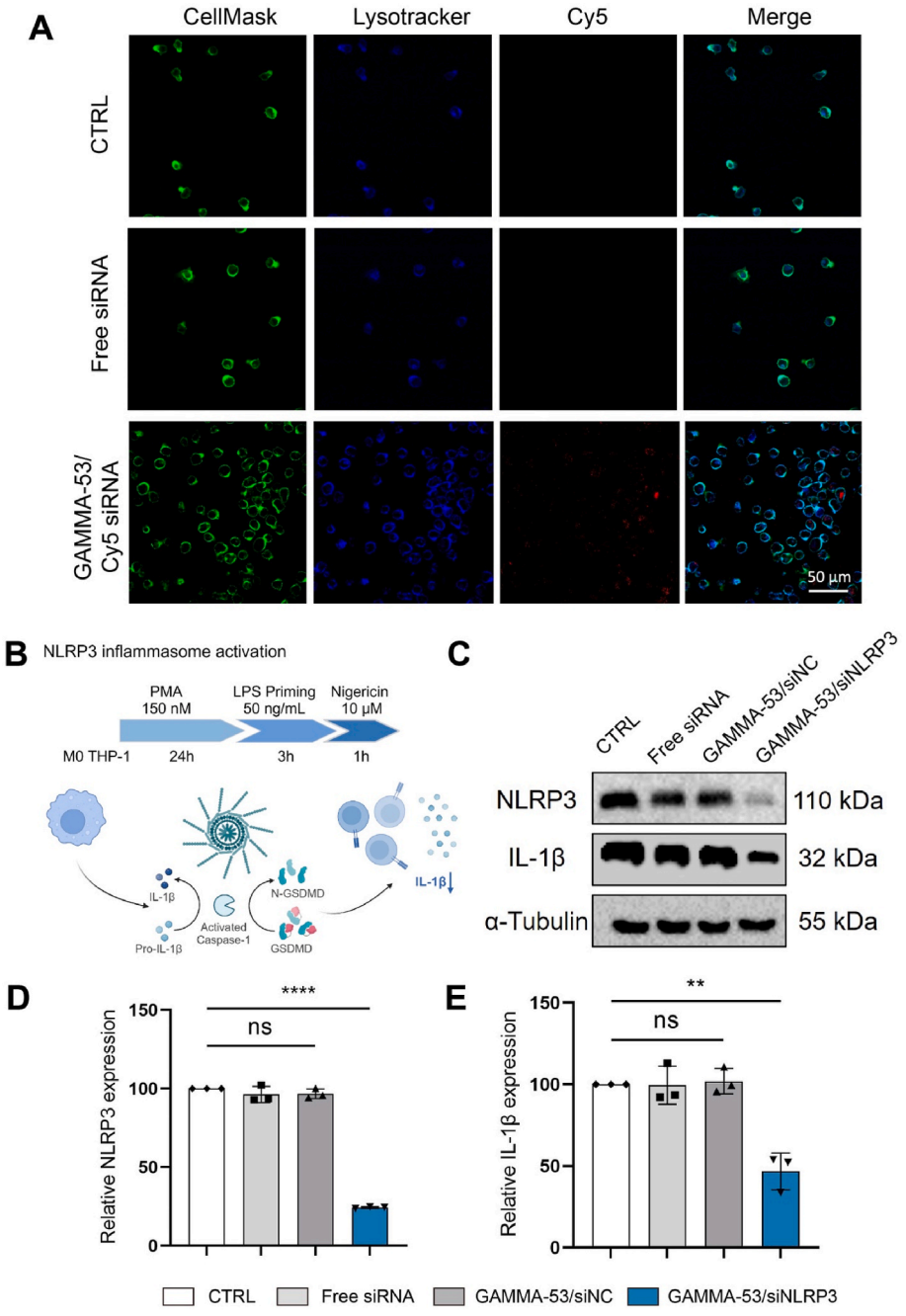

Fig. 5. GAMMA-53 NPs mediated siRNA delivery resolved NLRP3-dependent inflammation. (A) Confocal images showed the efficient endosomal escape of Cy5-siRNA mediated by GAMMA-53 NPs. **(B)** Schematic illustration of NLRP3 inflammasome activation and NLRP3-dependent innate immunity. **(C–E)** Western blotting analysis of expression of NLRP3, IL-1β and α-Tubulin after treatment with different formulations. Data is presented as mean ± SD. ns, no significance; **, $p < 0.01$; ****, $p < 0.0001$.

modulation of NLRP3 inflammasome. Human monocytic THP-1 cells was selected as model cell line, which contains the adaptor molecule apoptosis-associated speck-like protein (ASC) and the effector molecule caspase-1 [64]. The activation of NLRP3 inflammasome was executed following previously established protocols [41] as illustrated in Fig. 5B. RNAi therapeutics siNLRP3 was incorporated into GAMMA-53 (GAMMA-53/siNLRP3) at the concentration of 100 nM and then incubated with cells for 48 h. Afterwards, the protein expression levels of NLRP3 and IL-1β were detected via western blotting analysis. As shown in Fig. 5C–**D**, under the siNLRP3 concentration of 100 nM, significant suppression of NLRP3 expression (75.7 %) and IL-1β (53.3 %) were observed in the GAMMA-53/siNLRP3 group, whereas no statistically significant differences were noted among the control, free siNLRP3, and GAMMA-53/siNC groups (Fig. 5C–**E**), underscore the efficient NLRP3 inflammasome inhibitory capabilities mediated by GAMMA-53/siNLRP3.

3.6. Biosafety and enzymatic activity of GAMMA-53 NPs in ApoE$^{-/-}$ atherosclerosis mice

Next, we proceed with the *in vivo* evaluation of GAMMA-53 for potential AS treatment. Prior to this, the biosafety of GAMMA-53 was evaluated in healthy mice through intravenous administration of GAMMA-53 at the NPs dosage of 2.1 mg/kg. This concentration was chosen as it equates to an siRNA dosage of 0.1 mg/kg upon encapsulation, a level that will be utilized in the following *in vivo* therapeutic studies. Mice injected with PBS were served as control. 48 h post-injections, major organs including heart, liver, spleen, lung, and kidney were harvested for subsequent histological analysis. Hematoxylin and Eosin (H&E) staining revealed negligible difference between GAMMA-53 and PBS group in the microanatomical features of organs (Fig. 6A), suggesting the formulated GAMMA-53 were well tolerated in healthy mice, with no apparent histological tissue damage.

With the satisfied biosafety profile in healthy mice, we further tested the *in vivo* applicability of GAMMA-53 for AS mice [65]. To this end, a clinically relevant murine atherosclerotic model was chosen and apolipoprotein E–deficient (ApoE$^{-/-}$) mice was adopted, which was the most commonly used mice that are genetically modified to be more prone to developing the atherosclerosis [66]. Briefly, apolipoprotein-E-deficient (ApoE$^{-/-}$) mice were fed for western diet (WD) for 8 weeks and then intravenously injected with GAMMA-53 (2.1 mg/kg) or PBS twice a week for additional 6 weeks, during which the mice were maintained on the WD diet. Subsequently, the abdominal aortas were harvested for further analysis. Given the validated ROS elimination effects from GAMMA-53 *in vitro*, our initial focus was to test whether similar effects could be observed within the lesion area of the aortic root, which is

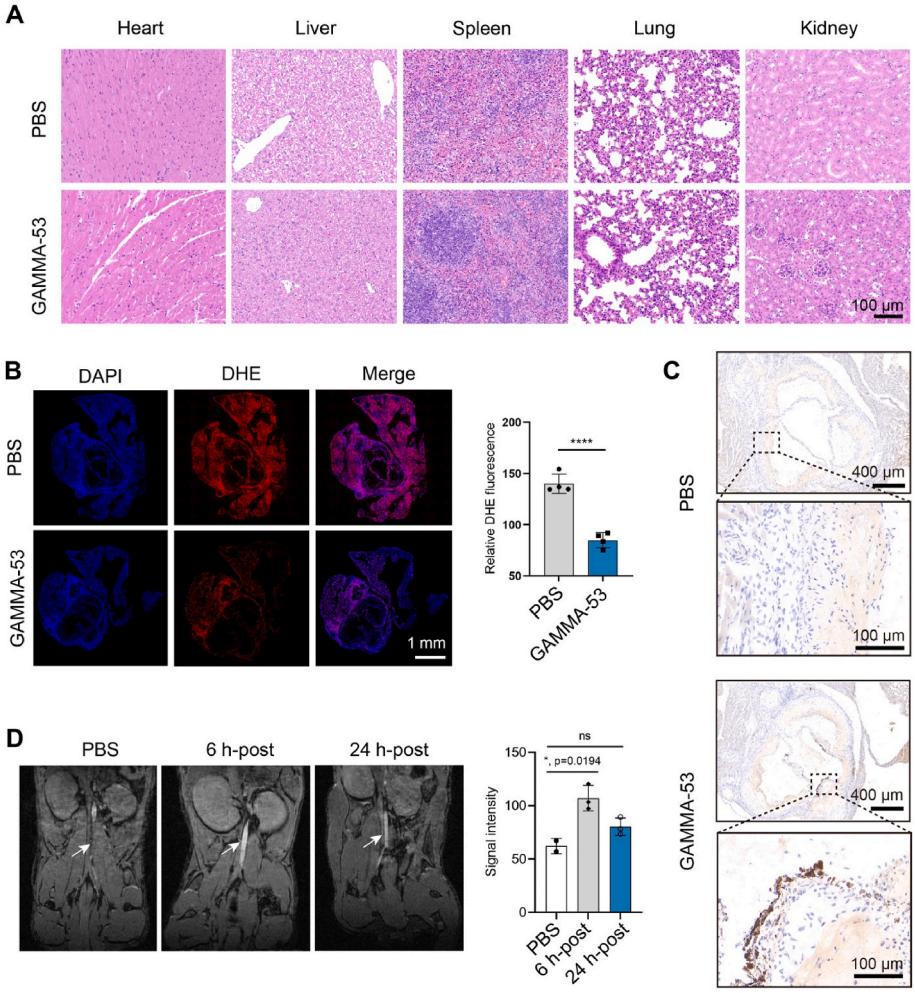

Fig. 6. Biological impact upon GAMMA-53 administration and the corresponding MR imaging potential. (A) Histological analysis of major organs after intravenous administration of GAMMA-53 for evaluating its biosafety profile evaluation of GAMMA-53 NPs after intravenously injection. **(B)** DHE staining in aortic root cross-sections to investigate the *in vivo* ROS elimination capability of GAMMA-53 within aortic root. **(C)** PPB staining evaluated the accumulation of GAMMA-53 in lesional areas in AS plaques. **(D)** Representative MRI images and quantified signal intensity post GAMMA-53 NPs injection. Data is presented as mean ± SD. ns, no significance; *, $p < 0.05$; ****, $p < 0.0001$.

known for the highest levels of oxidative stress throughout the progression of atherosclerosis [67]. The generation of ROS in aortic root cross sections was assayed by dihydroethidium (DHE) staining, and as shown in Fig. 6B, AS mice treated with GAMMA-53 resulted in a marked decrease in red fluorescent signal, demonstrating a 39.3 % reduction in comparison to the PBS-treated group, indicative of efficient ROS scavenge activity from GAMMA-53 *in vivo*.

3.7. AS targeting capacity of GAMMA-53 and its potential application for magnetic resonance imaging (MRI)

Subsequently, we aimed to investigate the potential accumulation of GAMMA-53 within AS plaques, a prerequisite for successful implementation of local inflammation attenuation [68]. Considering the backbone of the PBMMA-PG, β-glucan, is an inherent and precise targeting ligand of Dectin-1, we first evaluated the Dectin-1 expression profile in AS plaques [36,48]. Immunostaining for Dectin-1 in cross-sections of AS plaques revealed its marked expression, underscoring the participation Dectin-1^{+} cellular subsets in AS lesions (Fig. S9). This expression is a prerequisite for the efficient accumulation of GAMMA-53 within AS plaques. Taking advantage of the major iron composition of the GAMMA-53, we leveraged a label free method by employing the Perls Prussian blue (PPB) staining to investigate the accumulation of GAMMA-53 in AS plaque [10]. Histological

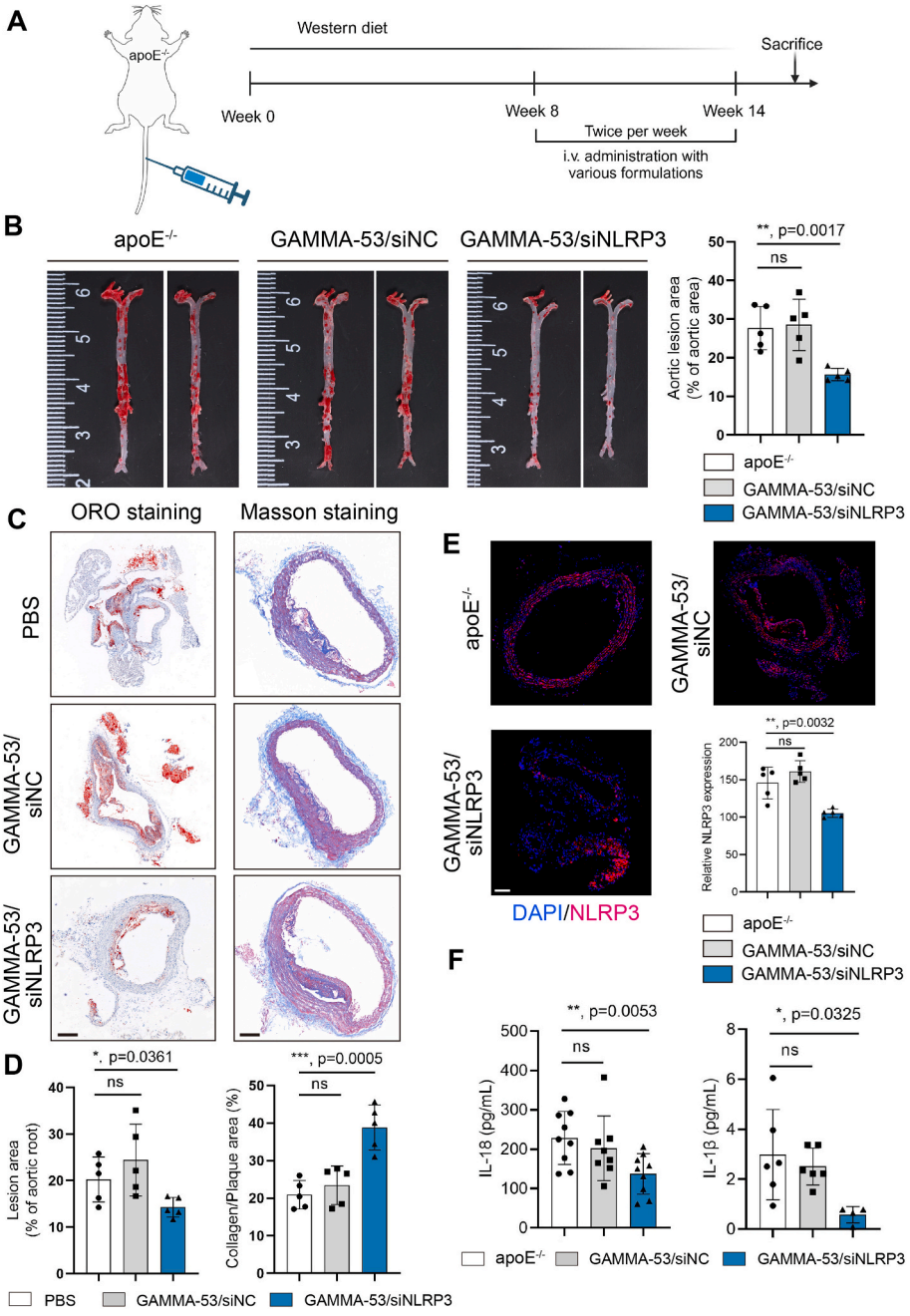

Fig. 7. Treatment with GAMMA-53/siNLRP3 NPs attenuate atherosclerosis via neutralizing NLRP3 inflammasome. (A) Schematic illustration of experimental design on therapeutic time course. **(B)** Representative ORO staining images of aorta and quantified to compare aortic lesion area in different groups. **(C)** ORO and Masson's trichrome staining were performed in aortic root cross-sections, and **(D)** quantitative evaluation was conducted to confirm the lesions and collagen cap thickness. **(E)** Immunostaining analysis of NLRP3 in aortic root cross-sections. **(F)** The expression levels of IL-1β and IL-18 cytokines were detected by ELISA assay. All scale bar equals 200 μm. Data is presented as mean ± SD. ns, no significance; *, $p < 0.05$; **, $p < 0.01$; ***, $p < 0.001$.

examination showed negligible iron deposition in the control aortic root, but positive staining in the lesion areas of mice treated with GAMMA-53 at a dosage of 2.1 mg/kg, suggesting enhanced GAMMA-53 accumulation within the plaques (Fig. 6C).

After confirming the major accumulation of GAMMA-53 in AS plaques, we further took advantage of the intrinsic properties of MIL-53 (Fe) as contrast agents for MR imaging, and examined whether or not the developed GAMMA-53 NPs was suitable for such diagnostic application. Mice with atherosclerosis were intravenously injected 0.8 mg of GAMMA-53, while mice injected with PBS were used as control. *In vivo* MR imaging was performed on a 7T Bruker Biospec System using a 3D gradient echo T1-weighted sequence. From the images, we noted a discernible signal along the abdominal aorta at multiple locations, which was augmented at the 6 h post-injection (Fig. 6D). Conversely, mice treated with PBS did not show a comparable signal. To quantify signal intensity (SI) showed in images, we calculated the normalized enhancement ratios (NER = $(SI_{post}\text{-}SI_{pre})/SI_{pre}$) using method described previously [69]. As indicated, the NER in the descending aorta was 0.7, suggesting the signal intensity increased by 72 % after GAMMA-53 NPs administration. Moreover, at 24 h after injection, although non-significant difference of signal intensity was observed compared to baseline, the NER still increased by 29 % as calculated.

Altogether, these results demonstrate the potential utility of targeted GAMMA-53 NPs for imaging inflammation within lesional macrophages, offering diagnostic capabilities for plaque identification.

3.8. GAMMA-53/siNLRP3 attenuate atherosclerotic injury via neutralizing NLRP3 inflammasome

We then evaluated the anti-atherosclerosis potential of GAMMA-53/siNLRP3. A schematic illustration of the therapeutic time course is depicted in Fig. 7A, where $ApoE^{-/-}$ mice were randomly divided into three groups and subjected to WD diet for 8 weeks. Following this period, groups were intravenously administered with either PBS, GAMMA-53/siNC or GAMMA-53/siNLRP3 at an siRNA dosage of 0.1 mg/kg, with treatments applied twice weekly for additional 6 weeks. At the end of the treatment, oil red O (ORO) staining was conducted to assess the atherosclerotic burden in aorta tissues, where AS plaques were indicated by the red regions. Fig. 7B revealed a clear AS plaque from PBS group, indicating the successful AS model establishment. Despite GAMMA-53 exhibited clear ROS elimination capacity in AS plaques (Fig. 6B), the treatment of GAMMA-53/siNC was unable to mount a significant reduction of plaque area. In contrast, treatment with GAMMA-53/siNLRP3 resulted in a significant anti-atherosclerotic effect, as evidenced by a 43.4 % reduction of plaque area. Consistent with the findings from the ORO assay across the entire aortic tissue, lesions within the aortic root of GAMMA-53/siNLRP3 treated mice also exhibited decreased ratios compared to the control groups (14.3 % *vs.* 20.2 %, $p < 0.05$), providing additional confirmation of the therapeutic efficacy mediated by GAMMA-53/siNLRP3 (Fig. 7C–D). As thin fibrous cap is known to exacerbate plaque vulnerability and increase the risk for acute cardiovascular events [70], thus the densely collagen-rich fibrous caps in aortic root from different groups were identified via Masson's Trichrome staining. A notable enhancement of fibrous cap thickness was observed in mice treated with GAMMA-53/siNLRP3 group compared to the control group (38.8 % *vs.* 20.9 %, $p < 0.0005$), whereas negligible differences were observed from GAMMA-53/siNC treatment, suggesting the retained atherosclerotic progression and better risk control from the GAMMA-53/siNLRP3 treatment (Fig. 7C–D).

To gain deeper insights into the inflammatory status upon GAMM-53/siNLRP3 treatment, we evaluated expression level of key components for NLRP3 inflammasome. The presence of NLRP3 was determined by immunostaining in the aortic root cross sections. Statistically significant suppression of NLRP3 expression (reduced by 27.6 %) was noted in mice treated with GAMMA-53/siNLRP3 NPs, indicative of efficient NLRP3 silencing in lesional site (Fig. 7E and separate channels in Fig. S10). Conversely, mice treated with PBS or GAMMA-53/siNC showed pervasive existence of NLRP3 in AS plaques, indicating the involvement of the NLRP3 inflammasomes activation during the progression of AS. IL-1β and IL-18 represent the major downstream cytokines resulting from NLRP3 inflammasome activation, which is tightly associated with the AS progression and immune homeostatic maintenance [71]. Therefore, we next evaluated serum level of IL-1β and IL-18 across various groups by enzyme-linked immunosorbent assay (ELISA) assay after 6 weeks of treatment. As shown in Fig. 7F, diminished secretion of serum IL-18 and IL-1β was evident in GAMMA-53/siNLRP3 treated mice, comparable to that observed in PBS and GAMMA-53/siNC groups.

Overall, the combined data demonstrate that the developed GAMMA-53 mediated RNAi therapeutics can effectively resolve the refractory pro-inflammatory microenvironment derived from aberrant NLRP3 inflammasome activation, further contributing to the AS progression management.

4. Discussion

Utilizing RNAi-anchored genetic tool to silence pathologic drivers in AS remains largely untapped due to the challenges of targeted delivery into lesional macrophages. An efficient siRNA delivery system for AS treatment should resolve several obstacles, including nuclease degradation, off-target effects, insufficient endosomal release, and poor plaque targeting [72,73]. Addressing these challenges concurrently can advance the genetic therapy for AS. Yet, despite the progressive achievements, the attainment of higher complexity and enhanced functionality in MOFs typically demands the incorporation of multiple components, which may further require complex synthesis procedures. Thus, the rational design and construction of delivery vehicle for AS genetic therapy should aim to offer a further simplified and facile approach, facilitating the production of multifunctional drug delivery system for AS management. Herein, a comprehensive study was designed to construct a simple, yet versatile MOF-based nanosystem through stepwise evaluation, proceeding through a sequential evaluation from initial NPs screening to ultimate *in vivo* application.

Initially, we chose iron-based MOF to be the core of the nanosystem in consideration of its satisfied biocompatibility, ROS scavenging properties and potential MR activities [29]. We successfully synthesized two iron-based MOFs, namely MIL-53 (Fe) and MIL-100 (Fe) for potential applications. However, it was noted that native frameworks showed unfavorable surface properties, such as limited colloidal stability and poor bioavailability [29]. Alternatively, coordinative external surface functionalization is highly desirable for conferring specific properties onto MOF NPs. Thus, we adopted a post-synthetic modification methodology as described previously [28], while tailoring the design and selection of a immuno-tropism polysaccharide specifically to fulfill the requirements of AS theranostics. The developed PBMMA-PG, mainly including 3 functional modulus, leverages a β-glucan backbone for selective targeting of atherosclerotic Dectin-1^{+} macrophages; phosphate groups for coordination with metal clusters, immobilizing the polymer on the host MOF; and PBMMA branches to grant the polymer pH-responsive morphological changes, enhancing endosomal escape. The successful coordination of PBMMA-PG on different MOF were well characterized, and the potential mechanism was also validated by a quantum chemical computation as well as MD simulation method. The tailored multifunctional design enables straightforward post-synthetic modification without complex physical encapsulation [31,74,75], embodying a modular strategy for the post-modification of MOF-based materials.

Afterwards, we conducted a systematic comparative analysis to evaluate the *in vitro* gene silencing behavior of PBMMA-PG modified MIL-53 (Fe) and MIL-100 (Fe), and the results indicated that PBMMA-PG modified MIL-53 (Fe), termed as GAMMA-53, surpassed its MIL-100 (Fe) counterpart in terms of cellular uptake efficiency, RNA encapsulation

efficiency, and gene silencing effectiveness. These results highlight that the selection of the MOF core substantially influences the nanosystem's biological performance in gene delivery upon the same surface modification. However, detailed investigations to unravel the underlying mechanisms for informed MOF selection needs continuous exploration.

Imaging of atherosclerotic plaque has evolved to include computed tomography (CT), MR imaging and positron emission tomography (PET), advancing a more detailed phenotyping of vulnerable atherosclerotic plaques [76]. Nevertheless, further enhancement in imaging resolution usually accounts for specific contrasting agents [68,76]. Leveraging the intrinsic properties of MIL-53 (Fe), the designed GAMMA-53 was utilized as a highly sensitive T1 contrast agent [77]. We have validated the effectiveness of GAMMA-53 as an imaging agent for enhancing the contrast in atherosclerotic plaque in a murine model. The AS plaque targeting capability can be attributed to the exclusive recognition of β-glucan, the backbone in PBMMA-PG, by Dectin-1^{+} macrophages, which are overly expressed within AS plaques [33,48]. Building on our previous studies using β-glucan based materials for delivering small molecules or nucleic acids to injured myocardium, the current study expands tailored design of β-glucan based polymers of into the realm of targeted imaging and precise delivery within atherosclerotic plaque tissues [36,48].

Characterized as an inflammatory disorder, AS entails a chronic progression marked by persistent hyperactivation of the innate immune system [78]. Recent studies identified NLRP3 inflammasome as a dominant mediator responsible for instigating inflammatory pathologies in atherosclerosis [71]. In such context, we demonstrated that the integration of NLRP3-targeted RNAi therapeutics into the engineered GAMMA-53 can attenuate its expression profile both *in vitro* and *in vivo*. The inhibition of NLRP3 inflammasome activation, coupled with the knockdown of NLRP3 by GAMMA-53/siNLRP3, resulted in favorable immunosuppression, leading to reduced secretion of the proinflammatory cytokines IL-1β and IL-18. Notably, despite the elevated oxidative stress observed in aortic plaques was alleviated by GAMMA-53 owing to its peroxidase activity, simply depleting the ROS production fail to mount a reduction in the AS plaque area and progression. Therefore, an improved molecular understanding of AS macrophages specific pathological signaling might further enable more effective AS management.

5. Conclusion

In summary, this study presents an easy and generalized "MOF-in-net" strategy for targeted siRNA delivery, the developed GAMMA-53 can concomitantly achieve robust gene interruption and theragnosis towards lesional macrophages, thereby holds potential for clinical translations and extend to other inflammatory indications. Featured with mild modification scheme, versatile functionalization choices, facile storage and re-disperse in aqueous solution, the findings herein may shed light on the application of MOF-mediated RNAi therapeutics in atherosclerosis.

Ethics approval and consent to participate

All the authors mentioned in the manuscript have agreed for authorship, read and approved the manuscript, and given consent for submission and subsequent publication of the manuscript. Animal studies involved in the manuscript has been approved by the Institutional Animal Care and Use Committee at School of Basic Medical Sciences of Zhejiang University (SYXK(zhe)2019–0011).

Data availability

All data needed to evaluate the conclusions in the paper are present in the paper and/or the Supplementary Materials.

CRediT authorship contribution statement

Sen Li: Investigation, Funding acquisition. **Han Gao:** Writing – review & editing, Writing – original draft, Supervision, Methodology, Investigation, Conceptualization. **Haoji Wang:** Methodology, Investigation. **Xiaolin Zhao:** Methodology, Investigation. **Da Pan:** Methodology, Investigation. **Idaira Pacheco-Fernández:** Methodology, Investigation. **Ming Ma:** Methodology, Investigation, Funding acquisition. **Jianjun Liu:** Methodology, Investigation. **Jouni Hirvonen:** Visualization, Supervision, Investigation. **Zehua Liu:** Writing – review & editing, Visualization, Supervision, Methodology, Investigation, Funding acquisition, Conceptualization. **Hélder A. Santos:** Writing – review & editing, Visualization, Validation, Supervision, Investigation, Funding acquisition, Conceptualization.

Declaration of competing interest

The authors declare that they have no known competing financial interests or personal relationships that could have appeared to influence the work reported in this paper.

Acknowledgements

S. Li acknowledges financial support from Seed Funding from Second Affiliated Hospital of Zhejiang University School of Medicine. Z. Liu acknowledges financial support from Academy of Finland (No. 340129) and Finnish Foundation for Cardiovascular Research. Prof. H. A. Santos acknowledges financial support from Academy of Finland (No. 331151) and the UMCG Research Funds. H. Gao acknowledges financial support from the Chinese Scholarship Council (No. 202006090004). I. Pacheco-Fernández acknowledges financial support European Union's Horizon Europe 2021 Research and Innovation Programme for her Marie Skłodowska-Curie (No. 101059391). M. Ma acknowledges financial support from National Natural Science Foundation of China (No. 52072392, 52472290). X. Zhao acknowledges the financial support from Shanghai Super Post-Doctor Incentive Program (No. 2022665).

Appendix A. Supplementary data

Supplementary data to this article can be found online at https://doi.org/10.1016/j.bioactmat.2024.08.041.

References

[1] S.E. Engelen, A.J.B. Robinson, Y.-X. Zurke, C. Monaco, Therapeutic strategies targeting inflammation and immunity in atherosclerosis: how to proceed? Nat. Rev. Cardiol. 19 (2022) 522–542, https://doi.org/10.1038/s41569-021-00668-4.
[2] M.T. Patterson, M.M. Firulyova, Y. Xu, H. Hillman, C. Bishop, A. Zhu, G.H. Hickok, P.R. Schrank, C.E. Ronayne, Z. Caillot, G. Fredrickson, A.E. Kennedy, N. Acharya, J. G. Neels, G. Chinetti, X. Revelo, I.M. Stromnes, S. Ivanov, T.D. Bold, K. Zaitsev, J. W. Williams, Trem2 promotes foamy macrophage lipid uptake and survival in atherosclerosis, Nature Cardiovascular Research 2 (2023) 1015–1031, https://doi.org/10.1038/s44161-023-00354-3.
[3] K.J. Moore, I. Tabas, Macrophages in the pathogenesis of atherosclerosis, Cell 145 (2011) 341–355, https://doi.org/10.1016/j.cell.2011.04.005.
[4] G.K. Hansson, P. Libby, I. Tabas, Inflammation and plaque vulnerability, J. Intern. Med. 278 (2015) 483–493, https://doi.org/10.1111/joim.12406.
[5] V. Stoneman, D. Braganza, N. Figg, J. Mercer, R. Lang, M. Goddard, M. Bennett, Monocyte/macrophage suppression in CD11b diphtheria toxin receptor transgenic mice differentially affects atherogenesis and established plaques, Circ. Res. 100 (2007) 884–893, https://doi.org/10.1161/01.Res.0000260802.75766.00.
[6] A.R. Tall, L. Yvan-Charvet, Cholesterol, inflammation and innate immunity, Nat. Rev. Immunol. 15 (2015) 104–116, https://doi.org/10.1038/nri3793.
[7] Z. Liu, S. Wang, C. Tapeinos, G. Torrieri, V. Kankanen, N. El-Sayed, A. Python, J. T. Hirvonen, H.A. Santos, Non-viral nanoparticles for RNA interference: principles of design and practical guidelines, Adv. Drug Deliv. Rev. (2021), https://doi.org/10.1016/j.addr.2021.05.018.
[8] O. Soehnlein, P. Libby, Targeting inflammation in atherosclerosis — from experimental insights to the clinic, Nat. Rev. Drug Discov. 20 (2021) 589–610, https://doi.org/10.1038/s41573-021-00198-1.

[9] W. Chen, M. Schilperoort, Y. Cao, J. Shi, I. Tabas, W. Tao, Macrophage-targeted nanomedicine for the diagnosis and treatment of atherosclerosis, Nat. Rev. Cardiol. 19 (2022) 228–249, https://doi.org/10.1038/s41569-021-00629-x.
[10] T. Baati, L. Njim, F. Neffati, A. Kerkeni, M. Bouttemi, R. Gref, M.F. Najjar, A. Zakhama, P. Couvreur, C. Serre, P. Horcajada, In depth analysis of the in vivo toxicity of nanoparticles of porous iron(iii) metal–organic frameworks, Chem. Sci. 4 (2013) 1597–1607, https://doi.org/10.1039/C3SC22116D.
[11] J. Joseph, S. Iftekhar, V. Srivastava, Z. Fallah, E.N. Zare, M. Sillanpää, Iron-based metal-organic framework: synthesis, structure and current technologies for water reclamation with deep insight into framework integrity, Chemosphere 284 (2021) 131171, https://doi.org/10.1016/j.chemosphere.2021.131171.
[12] X. Peng, L. Xu, M. Zeng, H. Dang, Application and development prospect of nanoscale iron based metal-organic frameworks in biomedicine, Int. J. Nanomed. 18 (2023) 4907–4931, https://doi.org/10.2147/IJN.S417543.
[13] R. Fu, Z. Ma, H. Zhao, H. Jin, Y. Tang, T. He, Y. Ding, J. Zhang, D. Ye, Research progress in iron-based nanozymes: catalytic mechanisms, classification, and biomedical applications, Anal. Chem. 95 (2023) 10844–10858, https://doi.org/10.1021/acs.analchem.3c01005.
[14] P. Qiu, M. Huang, S. Wu, M. Wen, N. Yu, Z. Chen, Dynamic effects of endo–exogenous stimulations on enzyme-activatable polymeric nanosystems with photo–sono–chemo synergy, ACS Appl. Mater. Interfaces 14 (2022) 29537–29549, https://doi.org/10.1021/acsami.2c05276.
[15] B. Zhang, Y. Gao, R. Yang, Z. Ouyang, H. Yu, H. Wang, X. Shi, M. Shen, Tumor-anchoring drug-loaded fibrous microspheres for MR imaging-guided local chemotherapy and metastasis inhibition, Advanced Fiber Materials 4 (2022) 807–819, https://doi.org/10.1007/s42765-022-00137-8.
[16] L. Chen, X. Sun, K. Cheng, P.D. Topham, M. Xu, Y. Jia, D. Dong, S. Wang, Y. Liu, L. Wang, Q. Yu, Temperature-regulating phase change fiber scaffold toward mild photothermal–chemotherapy, Advanced Fiber Materials 4 (2022) 1669–1684, https://doi.org/10.1007/s42765-022-00199-8.
[17] J. Yang, L. Xu, Y. Ding, C. Liu, B. Wang, Y. Yu, C. Hui, S. Ramakrishna, J. Zhang, Y. Long, NIR-II-Triggered composite nanofibers to simultaneously achieve intracranial hemostasis, killing superbug and residual cancer cells in brain tumor resection surgery, Advanced Fiber Materials 5 (2023) 209–222, https://doi.org/10.1007/s42765-022-00210-2.
[18] L. Guo, Y. Chen, T. Wang, Y. Yuan, Y. Yang, X. Luo, S. Hu, J. Ding, W. Zhou, Rational design of metal-organic frameworks to deliver methotrexate for targeted rheumatoid arthritis therapy, J. Contr. Release 330 (2021) 119–131, https://doi.org/10.1016/j.jconrel.2020.10.069.
[19] A.K. Bindra, D. Wang, Y. Zhao, Metal–organic frameworks meet polymers: from synthesis strategies to healthcare applications, Adv. Mater. 35 (2023) 2300700, https://doi.org/10.1002/adma.202300700.
[20] M. Pander, R. Gil-San-Millan, P. Delgado, C. Perona-Bermejo, U. Kostrzewa, K. Kaczkowski, D.J. Kubicki, J.A.R. Navarro, W. Bury, MOF/polymer hybrids through in situ free radical polymerization in metal-organic frameworks, Mater. Horiz. 10 (2023) 1301–1308, https://doi.org/10.1039/D2MH01202B.
[21] W. Zhu, G. Xiang, J. Shang, J. Guo, B. Motevalli, P. Durfee, J.O. Agola, E.N. Coker, C.J. Brinker, Versatile surface functionalization of metal–organic frameworks through direct metal coordination with a phenolic lipid enables diverse applications, Adv. Funct. Mater. 28 (2018) 1705274, https://doi.org/10.1002/adfm.201705274.
[22] H. Hu, Z. Wang, L. Cao, L. Zeng, C. Zhang, W. Lin, C. Wang, Metal–organic frameworks embedded in a liposome facilitate overall photocatalytic water splitting, Nat. Chem. 13 (2021) 358–366, https://doi.org/10.1038/s41557-020-00635-5.
[23] R. Cheng, L. Jiang, H. Gao, Z. Liu, E. Mäkilä, S. Wang, Q. Saiding, L. Xiang, X. Tang, M. Shi, J. Liu, L. Pang, J. Salonen, J. Hirvonen, H. Zhang, W. Cui, B. Shen, H. A. Santos, A pH-responsive cluster metal–organic framework nanoparticle for enhanced tumor accumulation and antitumor effect, Adv. Mater. 34 (2022) 2203915, https://doi.org/10.1002/adma.202203915.
[24] L. Dai, M. Yao, Z. Fu, X. Li, X. Zheng, S. Meng, Z. Yuan, K. Cai, H. Yang, Y. Zhao, Multifunctional metal-organic framework-based nanoreactor for starvation/oxidation improved indoleamine 2,3-dioxygenase-blockade tumor immunotherapy, Nat. Commun. 13 (2022) 2688, https://doi.org/10.1038/s41467-022-30436-y.
[25] S.V. Dummert, H. Saini, M.Z. Hussain, K. Yadava, K. Jayaramulu, A. Casini, R. A. Fischer, Cyclodextrin metal–organic frameworks and derivatives: recent developments and applications, Chem. Soc. Rev. 51 (2022) 5175–5213, https://doi.org/10.1039/D1CS00550B.
[26] S.H. Park, S.J. Lee, Versatile amorphous structures of phosphonate Metal−Organic framework/alginate composite for tunable sieving of ions, Adv. Funct. Mater. 29 (2019) 1904016, https://doi.org/10.1002/adfm.201904016.
[27] E. Khare, N. Holten-Andersen, M.J. Buehler, Transition-metal coordinate bonds for bioinspired macromolecules with tunable mechanical properties, Nat. Rev. Mater. 6 (2021) 421–436, https://doi.org/10.1038/s41578-020-00270-z.
[28] X. Chen, Y. Zhuang, N. Rampal, R. Hewitt, G. Divitini, C.A. O'Keefe, X. Liu, D. J. Whitaker, J.W. Wills, R. Jugdaohsingh, J.J. Powell, H. Yu, C.P. Grey, O. A. Scherman, D. Fairen-Jimenez, Formulation of metal–organic framework-based drug carriers by controlled coordination of methoxy PEG phosphate: boosting colloidal stability and redispersibility, J. Am. Chem. Soc. 143 (2021) 13557–13572, https://doi.org/10.1021/jacs.1c03943.
[29] Y. He, D. Li, L. Wu, X. Yin, X. Zhang, L.H. Patterson, J. Zhang, Metal-organic frameworks for gene therapy and detection, Adv. Funct. Mater. 33 (2023) 2212277, https://doi.org/10.1002/adfm.202212277.
[30] S. Wang, C.M. McGuirk, M.B. Ross, S. Wang, P. Chen, H. Xing, Y. Liu, C.A. Mirkin, General and direct method for preparing oligonucleotide-functionalized metal–organic framework nanoparticles, J. Am. Chem. Soc. 139 (2017) 9827–9830, https://doi.org/10.1021/jacs.7b05633.
[31] Z. Lin, J.J. Richardson, J. Zhou, F. Caruso, Direct synthesis of amorphous coordination polymers and metal–organic frameworks, Nat. Rev. Chem 7 (2023) 273–286, https://doi.org/10.1038/s41570-023-00474-1.
[32] Y. Meng, Y. Chen, J. Zhu, Y. Qi, J. Ding, W. Zhou, Polarity control of DNA adsorption enabling the surface functionalization of CuO nanozymes for targeted tumor therapy, Mater. Horiz. 8 (2021) 972–986, https://doi.org/10.1039/D0MH01372B.
[33] K. Szilagyi, M.J.J. Gijbels, S. van der Velden, S.E.M. Heinsbroek, G. Kraal, M.P.J. de Winther, T.K. van den Berg, Dectin-1 deficiency does not affect atherosclerosis development in mice, Atherosclerosis 239 (2015) 318–321, https://doi.org/10.1016/j.atherosclerosis.2015.02.005.
[34] A.M. Omer, E.M. Abd El-Monaem, G.M. El-Subruiti, M.M. Abd El-Latif, A. S. Eltaweil, Fabrication of easy separable and reusable MIL-125(Ti)/MIL-53(Fe) binary MOF/CNT/Alginate composite microbeads for tetracycline removal from water bodies, Sci. Rep. 11 (2021) 23818, https://doi.org/10.1038/s41598-021-03428-z.
[35] N.M. Mahmoodi, J. Abdi, M. Oveisi, M. Alinia Asli, M. Vossoughi, Metal-organic framework (MIL-100 (Fe)): synthesis, detailed photocatalytic dye degradation ability in colored textile wastewater and recycling, Mater. Res. Bull. 100 (2018) 357–366, https://doi.org/10.1016/j.materresbull.2017.12.033.
[36] Z. Liu, W. Lian, Q. Long, R. Cheng, G. Torrieri, B. Zhang, A. Koivuniemi, M. Mahmoudzadeh, A. Bunker, H. Gao, H. He, Y. Chen, J. Hirvonen, R. Zhou, Q. Zhao, X. Ye, X. Deng, H.A. Santos, Promoting cardiac repair through simple engineering of nanoparticles with exclusive targeting capability toward myocardial reperfusion injury by thermal resistant microfluidic platform, Adv. Funct. Mater. (2022), https://doi.org/10.1002/adfm.202204666.
[37] H. Willcock, R.K. O'Reilly, End group removal and modification of RAFT polymers, Polym. Chem. 1 (2010) 149–157, https://doi.org/10.1039/b9py00340a.
[38] T. Lu, Sobtop, 1.0(dev3.2), in.
[39] N.M. O'Boyle, M. Banck, C.A. James, C. Morley, T. Vandermeersch, G. R. Hutchison, Open Babel: an open chemical toolbox, J. Cheminf. 3 (2011) 33, https://doi.org/10.1186/1758-2946-3-33.
[40] Y. Sun, L. Zheng, Y. Yang, X. Qian, T. Fu, X. Li, Z. Yang, H. Yan, C. Cui, W. Tan, Metal–organic framework nanocarriers for drug delivery in biomedical applications, Nano-Micro Lett. 12 (2020) 103, https://doi.org/10.1007/s40820-020-00423-3.
[41] J. Chen, Z.J. Chen, PtdIns4P on dispersed trans-Golgi network mediates NLRP3 inflammasome activation, Nature 564 (2018) 71–76, https://doi.org/10.1038/s41586-018-0761-3.
[42] R. Ettlinger, U. Lächelt, R. Gref, P. Horcajada, T. Lammers, C. Serre, P. Couvreur, R. E. Morris, S. Wuttke, Toxicity of metal–organic framework nanoparticles: from essential analyses to potential applications, Chem. Soc. Rev. 51 (2022) 464–484, https://doi.org/10.1039/D1CS00918D.
[43] R. Nivetha, P. Kollu, K. Chandar, S. Pitchaimuthu, S.K. Jeong, A.N. Grace, Role of MIL-53(Fe)/hydrated–dehydrated MOF catalyst for electrochemical hydrogen evolution reaction (HER) in alkaline medium and photocatalysis, RSC Adv. 9 (2019) 3215–3223, https://doi.org/10.1039/C8RA08208A.
[44] S. Wang, C.M. McGuirk, A. d'Aquino, J.A. Mason, C.A. Mirkin, Metal–organic framework nanoparticles, Adv. Mater. 30 (2018) 1800202, https://doi.org/10.1002/adma.201800202.
[45] Y. Liang, X. Yang, X. Wang, Z.-J. Guan, H. Xing, Y. Fang, A cage-on-MOF strategy to coordinatively functionalize mesoporous MOFs for manipulating selectivity in adsorption and catalysis, Nat. Commun. 14 (2023) 5223, https://doi.org/10.1038/s41467-023-40973-9.
[46] W. Yin, Z. Xu, C. Chang, Y. Zhao, H. Wang, J. Zhang, F. Ma, X. Zuo, B. Tang, Y. Lu, Alginate di-aldehyde-modified metal-organic framework nanocarriers as delivery platform and adjuvant in inactivated pseudorabies vaccination, Mater. Horiz. (2024), https://doi.org/10.1039/d3mh02251j.
[47] K. Szilagyi, M.J. Gijbels, S. van der Velden, S.E. Heinsbroek, G. Kraal, M.P. de Winther, T.K. van den Berg, Dectin-1 deficiency does not affect atherosclerosis development in mice, Atherosclerosis 239 (2015) 318–321, https://doi.org/10.1016/j.atherosclerosis.2015.02.005.
[48] H. Gao, S. Wang, Q. Long, R. Cheng, W. Lian, A. Koivuniemi, M. Ma, B. Zhang, J. Hirvonen, X. Deng, Z. Liu, X. Ye, H.A. Santos, Rational design of a polysaccharide-based viral mimicry nanocomplex for potent gene silencing in inflammatory tissues, J. Contr. Release 357 (2023) 120–132, https://doi.org/10.1016/j.jconrel.2023.03.037.
[49] X. Wang, Y. Hu, Y. Tang, P. Yang, X. Feng, W. Xu, M. Zhu, Phosphate and phytate adsorption and precipitation on ferrihydrite surfaces, Environ. Sci.: Nano 4 (2017) 2193–2204, https://doi.org/10.1039/C7EN00705A.
[50] M.J. Frisch, G.W. Trucks, H.B. Schlegel, G.E. Scuseria, M.A. Robb, J.R. Cheeseman, G. Scalmani, V. Barone, G.A. Petersson, H. Nakatsuji, X. Li, M. Caricato, A. V. Marenich, J. Bloino, B.G. Janesko, R. Gomperts, B. Mennucci, H.P. Hratchian, J. V. Ortiz, A.F. Izmaylov, J.L. Sonnenberg, Williams, F. Ding, F. Lipparini, F. Egidi, J. Goings, B. Peng, A. Petrone, T. Henderson, D. Ranasinghe, V.G. Zakrzewski, J. Gao, N. Rega, G. Zheng, W. Liang, M. Hada, M. Ehara, K. Toyota, R. Fukuda, J. Hasegawa, M. Ishida, T. Nakajima, Y. Honda, O. Kitao, H. Nakai, T. Vreven, K. Throssell, J.A. Montgomery Jr., J.E. Peralta, F. Ogliaro, M.J. Bearpark, J. J. Heyd, E.N. Brothers, K.N. Kudin, V.N. Staroverov, T.A. Keith, R. Kobayashi, J. Normand, K. Raghavachari, A.P. Rendell, J.C. Burant, S.S. Iyengar, J. Tomasi, M. Cossi, J.M. Millam, M. Klene, C. Adamo, R. Cammi, J.W. Ochterski, R.L. Martin, K. Morokuma, O. Farkas, J.B. Foresman, D.J. Fox, Gaussian 16 Rev. A. 1 (2016). Wallingford, CT.

[51] C. Lee, W. Yang, R.G. Parr, Development of the Colle-Salvetti correlation-energy formula into a functional of the electron density, Phys. Rev. B Condens. Matter 37 (1988) 785–789, https://doi.org/10.1103/physrevb.37.785.
[52] V. Gogonea, P.v.R. Schleyer, P.R. Schreiner, Consequences of triplet aromaticity in 4nπ-electron annulenes: calculation of magnetic shieldings for open-shell species, Angew. Chem. Int. Ed. 37 (1998) 1945–1948, https://doi.org/10.1002/(SICI)1521-3773(19980803)37:13/14<1945::AID-ANIE1945>3.0.CO;2-E.
[53] T. Lu, F. Chen, Multiwfn: a multifunctional wavefunction analyzer, J. Comput. Chem. 33 (2012) 580–592, https://doi.org/10.1002/jcc.22885.
[54] S. Wannasarit, S. Wang, P. Figueiredo, C. Trujillo, F. Eburnea, L. Simón-Gracia, A. Correia, Y. Ding, T. Teesalu, D. Liu, R. Wiwattanapatapee, H.A. Santos, W. Li, A virus-mimicking pH-responsive acetalated dextran-based membrane-active polymeric nanoparticle for intracellular delivery of antitumor therapeutics, Adv. Funct. Mater. 29 (2019), https://doi.org/10.1002/adfm.201905352.
[55] D. Van Der Spoel, E. Lindahl, B. Hess, G. Groenhof, A.E. Mark, H.J. Berendsen, GROMACS: fast, flexible, and free, J. Comput. Chem. 26 (2005) 1701–1718, https://doi.org/10.1002/jcc.20291.
[56] P.K. Yuet, D. Blankschtein, Molecular dynamics simulation study of water surfaces: comparison of flexible water models, J. Phys. Chem. B 114 (2010) 13786–13795, https://doi.org/10.1021/jp1067022.
[57] M. Fischer, J.P. Müller, B. Spies-Weisshart, C. Gräfe, O. Kurzai, K. Hünniger, A. Hochhaus, S. Scholl, U. Schnetzke, Isoform localization of Dectin-1 regulates the signaling quality of anti-fungal immunity, Eur. J. Immunol. 47 (2017) 848–859, https://doi.org/10.1002/eji.201646849.
[58] H.S. Goodridge, C.N. Reyes, C.A. Becker, T.R. Katsumoto, J. Ma, A.J. Wolf, N. Bose, A.S. Chan, A.S. Magee, M.E. Danielson, A. Weiss, J.P. Vasilakos, D.M. Underhill, Activation of the innate immune receptor Dectin-1 upon formation of a 'phagocytic synapse', Nature 472 (2011) 471–475, https://doi.org/10.1038/nature10071.
[59] Y. Dorsett, T. Tuschl, siRNAs: applications in functional genomics and potential as therapeutics, Nat. Rev. Drug Discov. 3 (2004) 318–329, https://doi.org/10.1038/nrd1345.
[60] W. Dong, X. Liu, W. Shi, Y. Huang, Metal–organic framework MIL-53(Fe): facile microwave-assisted synthesis and use as a highly active peroxidase mimetic for glucose biosensing, RSC Adv. 5 (2015) 17451–17457, https://doi.org/10.1039/C4RA15840G.
[61] E. Eruslanov, S. Kusmartsev, Identification of ROS using oxidized DCFDA and flow-cytometry, Methods Mol. Biol. 594 (2010) 57–72, https://doi.org/10.1007/978-1-60761-411-1_4.
[62] P.M. Ridker, B.M. Everett, T. Thuren, J.G. MacFadyen, W.H. Chang, C. Ballantyne, F. Fonseca, J. Nicolau, W. Koenig, S.D. Anker, J.J.P. Kastelein, J.H. Cornel, P. Pais, D. Pella, J. Genest, R. Cifkova, A. Lorenzatti, T. Forster, Z. Kobalava, L. Vida-Simiti, M. Flather, H. Shimokawa, H. Ogawa, M. Dellborg, P.R.F. Rossi, R.P.T. Troquay, P. Libby, R.J. Glynn, Antiinflammatory therapy with canakinumab for atherosclerotic disease, N. Engl. J. Med. 377 (2017) 1119–1131, https://doi.org/10.1056/NEJMoa1707914.
[63] J.C. Tardif, S. Kouz, D.D. Waters, O.F. Bertrand, R. Diaz, A.P. Maggioni, F.J. Pinto, R. Ibrahim, H. Gamra, G.S. Kiwan, C. Berry, J. López-Sendón, P. Ostadal, W. Koenig, D. Angoulvant, J.C. Grégoire, M.A. Lavoie, M.P. Dubé, D. Rhainds, M. Provencher, L. Blondeau, A. Orfanos, P.L. L'Allier, M.C. Guertin, F. Roubille, Efficacy and safety of low-dose colchicine after myocardial infarction, N. Engl. J. Med. 381 (2019) 2497–2505, https://doi.org/10.1056/NEJMoa1912388.
[64] J.H. Kim, H.J. Sohn, J.K. Yoo, H. Kang, G.S. Seong, Y.J. Chwae, K. Kim, S. Park, H. J. Shin, NLRP3 inflammasome activation in THP-1 target cells triggered by pathogenic naegleria fowleri, Infect. Immun. 84 (2016) 2422–2428, https://doi.org/10.1128/iai.00275-16.
[65] A. Gisterå, D.F.J. Ketelhuth, S.G. Malin, G.K. Hansson, Animal models of atherosclerosis–supportive notes and tricks of the trade, Circ. Res. 130 (2022) 1869–1887, https://doi.org/10.1161/CIRCRESAHA.122.320263.
[66] G.S. Getz, C.A. Reardon, Diet and murine atherosclerosis, Arterioscler. Thromb. Vasc. Biol. 26 (2006) 242–249, https://doi.org/10.1161/01.Atv.0000201071.49029.17.
[67] W.N. Nowak, J. Deng, X.Z. Ruan, Q. Xu, Reactive oxygen species generation and atherosclerosis, Arterioscler. Thromb. Vasc. Biol. 37 (2017) e41–e52, https://doi.org/10.1161/ATVBAHA.117.309228.
[68] D.G. Woodside, E.A. Tanifum, K.B. Ghaghada, R.J. Biediger, A.R. Caivano, Z. A. Starosolski, S. Khounlo, S. Bhayana, S. Abbasi, J.W. Craft, D.S. Maxwell, C. Patel, I.V. Stupin, D. Bakthavatsalam, R.V. Market, J.T. Willerson, R.A.F. Dixon, P. Vanderslice, A.V. Annapragada, Magnetic resonance imaging of atherosclerotic plaque at clinically relevant field strengths (1T) by targeting the integrin α4β1, Sci. Rep. 8 (2018) 3733, https://doi.org/10.1038/s41598-018-21893-x.
[69] W. Chen, D.P. Cormode, Y. Vengrenyuk, B. Herranz, J.E. Feig, A. Klink, W.J. M. Mulder, E.A. Fisher, Z.A. Fayad, Collagen-specific peptide conjugated HDL nanoparticles as MRI contrast agent to evaluate compositional changes in atherosclerotic plaque regression, JACC (J. Am. Coll. Cardiol.): Cardiovascular Imaging 6 (2013) 373–384, https://doi.org/10.1016/j.jcmg.2012.06.016.
[70] A.V. Finn, M. Nakano, J. Narula, F.D. Kolodgie, R. Virmani, Concept of vulnerable/unstable plaque, Arterioscler. Thromb. Vasc. Biol. 30 (2010) 1282–1292, https://doi.org/10.1161/ATVBAHA.108.179739.
[71] A. Christ, P. Günther, M.A.R. Lauterbach, P. Duewell, D. Biswas, K. Pelka, C. J. Scholz, M. Oosting, K. Haendler, K. Baßler, K. Klee, J. Schulte-Schrepping, T. Ulas, S.J.C.F.M. Moorlag, V. Kumar, M.H. Park, L.A.B. Joosten, L.A. Groh, N. P. Riksen, T. Espevik, A. Schlitzer, Y. Li, M.L. Fitzgerald, M.G. Netea, J.L. Schultze, E. Latz, Western diet triggers NLRP3-dependent innate immune reprogramming, Cell 172 (2018) 162–175.e114, https://doi.org/10.1016/j.cell.2017.12.013.
[72] Y. Dong, D.J. Siegwart, D.G. Anderson, Strategies, design, and chemistry in siRNA delivery systems, Adv. Drug Deliv. Rev. 144 (2019) 133–147, https://doi.org/10.1016/j.addr.2019.05.004.
[73] W. Tao, A. Yurdagul, N. Kong, W. Li, X. Wang, A.C. Doran, C. Feng, J. Wang, M. A. Islam, O.C. Farokhzad, I. Tabas, J. Shi, siRNA nanoparticles targeting CaMKIIγ in lesional macrophages improve atherosclerotic plaque stability in mice, Sci. Transl. Med. 12 (2020) eaay1063, https://doi.org/10.1126/scitranslmed.aay1063.
[74] Z. Liu, Y. Li, W. Li, C. Xiao, D. Liu, C. Dong, M. Zhang, E. Mäkilä, M. Kemell, J. Salonen, J.T. Hirvonen, H. Zhang, D. Zhou, X. Deng, H.A. Santos, Multifunctional nanohybrid based on porous silicon nanoparticles, gold nanoparticles, and acetalated dextran for liver regeneration and acute liver failure theranostics, Adv. Mater. 30 (2018) 1703393, https://doi.org/10.1002/adma.201703393.
[75] Q. Long, Z. Liu, Q. Shao, H. Shi, S. Huang, C. Jiang, B. Qian, Y. Zhong, X. He, X. Xiang, Y. Yang, B. Li, X. Yan, Q. Zhao, X. Wei, H.A. Santos, X. Ye, Autologous skin fibroblast-based PLGA nanoparticles for treating multiorgan fibrosis, Adv. Sci. 9 (2022) 2200856, https://doi.org/10.1002/advs.202200856.
[76] M.L. Senders, C. Calcagno, A. Tawakol, M. Nahrendorf, W.J.M. Mulder, Z.A. Fayad, PET/MR imaging of inflammation in atherosclerosis, Nat. Biomed. Eng. 7 (2023) 202–220, https://doi.org/10.1038/s41551-022-00970-7.
[77] M.A. Chowdhury, Metal-organic-frameworks as contrast agents in magnetic resonance imaging, ChemBioEng Rev. 4 (2017) 225–239, https://doi.org/10.1002/cben.201600027.
[78] D. Flores-Gomez, S. Bekkering, M.G. Netea, N.P. Riksen, Trained immunity in atherosclerotic cardiovascular disease, Arterioscler. Thromb. Vasc. Biol. 41 (2021) 62–69, https://doi.org/10.1161/ATVBAHA.120.314216.